

University of Groningen

Deuterated water in the solar-type protostars NGC 1333 IRAS 4A and IRAS 4B

Coutens, A.; Vastel, C.; Cabrit, S.; Codella, C.; Kristensen, L. E.; Ceccarelli, C.; van Dishoeck, E. F.; Boogert, A. C. A.; Bottinelli, S.; Castets, A.

Published in:
Astronomy and astrophysics

DOI:
[10.1051/0004-6361/201322400](https://doi.org/10.1051/0004-6361/201322400)

IMPORTANT NOTE: You are advised to consult the publisher's version (publisher's PDF) if you wish to cite from it. Please check the document version below.

Document Version
Publisher's PDF, also known as Version of record

Publication date:
2013

[Link to publication in University of Groningen/UMCG research database](#)

Citation for published version (APA):

Coutens, A., Vastel, C., Cabrit, S., Codella, C., Kristensen, L. E., Ceccarelli, C., van Dishoeck, E. F., Boogert, A. C. A., Bottinelli, S., Castets, A., Caux, E., Comito, C., Demyk, K., Herpin, F., Lefloch, B., McCoey, C., Mottram, J. C., Parise, B., Taquet, V., ... Yıldız, U. A. (2013). Deuterated water in the solar-type protostars NGC 1333 IRAS 4A and IRAS 4B. *Astronomy and astrophysics*, 560, [A39].
<https://doi.org/10.1051/0004-6361/201322400>

Copyright

Other than for strictly personal use, it is not permitted to download or to forward/distribute the text or part of it without the consent of the author(s) and/or copyright holder(s), unless the work is under an open content license (like Creative Commons).

The publication may also be distributed here under the terms of Article 25fa of the Dutch Copyright Act, indicated by the "Taverne" license. More information can be found on the University of Groningen website: <https://www.rug.nl/library/open-access/self-archiving-pure/taverne-amendment>.

Take-down policy

If you believe that this document breaches copyright please contact us providing details, and we will remove access to the work immediately and investigate your claim.

Downloaded from the University of Groningen/UMCG research database (Pure): <http://www.rug.nl/research/portal>. For technical reasons the number of authors shown on this cover page is limited to 10 maximum.

Deuterated water in the solar-type protostars NGC 1333 IRAS 4A and IRAS 4B^{★,★★}

A. Coutens^{1,2,3,4}, C. Vastel^{1,2}, S. Cabrit⁵, C. Codella⁶, L. E. Kristensen⁷, C. Ceccarelli⁸, E. F. van Dishoeck^{9,10},
 A. C. A. Boogert¹¹, S. Bottinelli^{1,2}, A. Castets⁸, E. Caux^{1,2}, C. Comito^{14,15}, K. Demyk^{1,2}, F. Herpin^{12,13}, B. Lefloch⁸,
 C. McCoey¹⁶, J. C. Mottram⁹, B. Parise¹⁵, V. Taquet¹⁷, F. F. S. van der Tak^{18,19}, R. Visser²⁰, and U. A. Yıldız⁹

(Affiliations can be found after the references)

Received 30 July 2013 / Accepted 21 October 2013

ABSTRACT

Context. The measure of the water deuterium fractionation is a relevant tool for understanding mechanisms of water formation and evolution from the prestellar phase to the formation of planets and comets.

Aims. The aim of this paper is to study deuterated water in the solar-type protostars NGC 1333 IRAS 4A and IRAS 4B, to compare their HDO abundance distributions with other star-forming regions, and to constrain their HDO/H₂O abundance ratios.

Methods. Using the *Herschel*/HIFI instrument as well as ground-based telescopes, we observed several HDO lines covering a large excitation range ($E_{\text{up}}/k = 22\text{--}168$ K) towards these protostars and an outflow position. Non-local thermal equilibrium radiative transfer codes were then used to determine the HDO abundance profiles in these sources.

Results. The HDO fundamental line profiles show a very broad component, tracing the molecular outflows, in addition to a narrower emission component and a narrow absorbing component. In the protostellar envelope of NGC 1333 IRAS 4A, the HDO inner ($T \geq 100$ K) and outer ($T < 100$ K) abundances with respect to H₂ are estimated with a 3σ uncertainty at $7.5^{+3.5}_{-3.0} \times 10^{-9}$ and $1.2^{+0.4}_{-0.4} \times 10^{-11}$, respectively, whereas in NGC 1333 IRAS 4B they are $1^{+1.8}_{-0.9} \times 10^{-8}$ and $1.2^{+0.6}_{-0.4} \times 10^{-10}$, respectively. Similarly to the low-mass protostar IRAS 16293-2422, an absorbing outer layer with an enhanced abundance of deuterated water is required to reproduce the absorbing components seen in the fundamental lines at 465 and 894 GHz in both sources. This water-rich layer is probably extended enough to encompass the two sources, as well as parts of the outflows. In the outflows emanating from NGC 1333 IRAS 4A, the HDO column density is estimated at about $(2\text{--}4) \times 10^{13}$ cm⁻², leading to an abundance of about $(0.7\text{--}1.9) \times 10^{-9}$. An HDO/H₂O ratio between 7×10^{-4} and 9×10^{-2} is also derived in the outflows. In the warm inner regions of these two sources, we estimate the HDO/H₂O ratios at about $1 \times 10^{-4}\text{--}4 \times 10^{-3}$. This ratio seems higher (a few %) in the cold envelope of IRAS 4A, whose possible origin is discussed in relation to formation processes of HDO and H₂O.

Conclusions. In low-mass protostars, the HDO outer abundances range in a small interval, between $\sim 10^{-11}$ and a few 10^{-10} . No clear trends are found between the HDO abundance and various source parameters (L_{bol} , L_{submm} , $L_{\text{submm}}/L_{\text{bol}}$, T_{bol} , $L_{\text{bol}}^{0.6}/M_{\text{env}}$). A tentative correlation is observed, however, between the ratio of the inner and outer abundances with the submillimeter luminosity.

Key words. astrochemistry – ISM: individual objects: NGC 1333 IRAS 4A – ISM: individual objects: NGC 1333 IRAS 4B – ISM: abundances – ISM: molecules

1. Introduction

The study of the deuterated isotopologues of water, HDO and D₂O, is helpful in order to understand water chemistry in the interstellar medium. Indeed, the HDO/H₂O¹ ratio can be used to constrain the water formation conditions. Water can be formed

by different mechanisms, both in the gas phase and on grain surfaces. In diffuse clouds, gas-phase ion-molecule reactions lead to the formation of the H₃O⁺ ion, which can dissociatively recombine to form H₂O (e.g., Dalgarno 1980; Jensen et al. 2000). Water can also form in the gas phase through the endothermic reaction of O with H₂ to form OH, followed by the reaction between OH and H₂ (e.g., Wagner & Graff 1987). Because of the endothermicity of the first reaction (~ 2000 K) and the high energy barrier of the second reaction (~ 2100 K), this mechanism is only important in regions with high temperatures (> 230 K), such as hot cores and shocks (Ceccarelli et al. 1996; Hollenbach & McKee 1979). In cold and dense regions, water is mainly formed by grain-surface chemistry, through hydrogenation of atomic and molecular oxygen accreted on the grains (e.g., Tielens & Hagen 1982; Ioppolo et al. 2008; Miyauchi et al. 2008; Dulieu et al. 2010; Cazaux et al. 2010). Water can then be thermally desorbed when the temperature is higher than ~ 100 K (Fraser et al. 2001), for example in the inner parts of the low-mass protostellar envelopes. It can also be released into the gas phase by non-thermal desorption mechanisms such as mechanical erosion (sputtering) in shocks (e.g., Flower & Pineau des Forêts 1994), or photodesorption by the interstellar radiation field or

[★] Based on observations carried out with the *Herschel*/HIFI instrument, the Institut de Radioastronomie Millimétrique (IRAM) 30 m Telescope, the *James Clerk Maxwell* Telescope (JCMT), and one of the ESO telescopes at the La Silla Paranal, the Atacama Pathfinder Experiment (APEX, programme ID 090.C-0239). *Herschel* is an ESA space observatory with science instruments provided by European-led principal Investigator consortia and with important participation from NASA. IRAM is supported by INSU/CNRS (France), MPG (Germany), and IGN (Spain). The JCMT is operated by the Joint Astronomy Centre on behalf of the Science and Technology Facilities Council of the United Kingdom, the Netherlands Organization for Scientific Research, and the National Research Council of Canada. APEX is a collaboration between the Max-Planck-Institut für Radioastronomie, the ESO, and the Onsala Space Observatory.

^{★★} Appendices are available in electronic form at <http://www.aanda.org>

¹ The HDO/H₂O ratio refers to twice the water D/H abundance ratio.

the cosmic ray induced UV-field (e.g., Öberg et al. 2009; Caselli et al. 2012). Deuterated water is expected to be formed in a similar way, but because of deuterium fractionation effects (e.g., Phillips & Vastel 2003), the HDO/H₂O ratio is dependent on the temperature at which the water formation takes place. This ratio should then be high if water forms at low temperatures, whereas it should be low if water forms at high temperatures.

In the past decade, many attempts have been made to explain the origin of Earth's water. Its formation may be endogenous or exogenous: water adsorbed on dry silicate grains in the protosolar nebula (Stimpfl et al. 2004), delivery through asteroids, comets, planetary embryos, and planetesimals (Morbidelli et al. 2000; O'Brien et al. 2006; Raymond et al. 2004, 2006, 2009; Lunine et al. 2003; Drake & Campins 2006), and water production through oxidation of a hydrogen rich atmosphere (Ikoma & Genda 2006). These sources can be investigated by studying the water D/H ratio. For example, the value toward eight Oort Cloud comets is, on average, twice that of the standard mean ocean water (SMOW, 1.56×10^{-4}) and 12 times the value of the D/H ratio in the early solar nebula ($\sim 2.5 \times 10^{-5}$; Niemann et al. 1996; Geiss & Gloeckler 1998). This difference led to the conclusion that comets were not the main source of the delivery of water to Earth (e.g., Bockelée-Morvan et al. 1998; Meier et al. 1998; Villanueva et al. 2009), although the original value of the D/H ratio of the Earth's water is unknown, and it is unclear how that value changed during the geophysical and geochemical evolution of the Earth (Campins & Lauretta 2004; Genda & Ikoma 2008). Recently, the water D/H ratio was measured with the HIFI spectrometer (Heterodyne Instrument for Far Infrared; de Graauw et al. 2010) onboard the *Herschel* Space Observatory (Pilbratt et al. 2010) to 1.61×10^{-4} in the Jupiter-family comet 103P/Hartley2 (Hartogh et al. 2011), close to the isotopic ratio measured in the Earth's oceans (1.5×10^{-4} ; Lecuyer et al. 1998). The determination of the HDO/H₂O ratio at different stages of the star formation process is then a way to determine how water evolves from the cold prestellar phase to the formation of planets and comets.

Until now, the HDO/H₂O ratio has been determined in four Class 0 protostars, corresponding to the main accretion phase. At this stage, the results are quite disparate. For example, in the warm inner regions ($T > 100$ K) of IRAS 16293-2422, Parise et al. (2005) and Coutens et al. (2012, 2013) estimated a warm HDO/H₂O ratio², at about a few percent, using single-dish observations, whereas Persson et al. (2013) found a much lower estimate ($\sim 9 \times 10^{-4}$) using interferometric data. This source is not the only one to present divergent results that depend on the studies. Indeed, the HDO/H₂O ratio in the warm inner envelope of NGC 1333 IRAS 2A, first estimated by Liu et al. (2011) at $\geq 1\%$, was determined at about 1×10^{-3} after revision of the H₂O abundance by Visser et al. (2013). This result remains different from another estimate, $(0.3\text{--}8) \times 10^{-2}$, by Taquet et al. (2013a). In NGC 1333 IRAS 4A (hereafter IRAS 4A) and NGC 1333 IRAS 4B (hereafter IRAS 4B), fewer studies have been carried out and are only based on interferometric observations. In IRAS 4A, Taquet et al. (2013a) found a ratio of 5×10^{-3} – 3×10^{-2} , and in IRAS 4B, Jørgensen & van Dishoeck (2010a) derived an upper limit of $\sim 6 \times 10^{-4}$. For more details on the results of the different studies of HDO/H₂O ratios in Class 0 sources and their type of analysis, we refer the reader

to Table 4 and Sect. 4.2. Singly deuterated water has also been studied in ices. Only upper limits between 5×10^{-3} and 2×10^{-2} have been determined (Parise et al. 2003; Dartois et al. 2003), which do not allow us to conclude on rather high ($\sim 10^{-2}$) or low ($\lesssim 10^{-3}$) HDO/H₂O ratios in grain mantles.

Even if it is not possible to disentangle the emission from the hot corino (defined as the warm inner part of the envelope in which complex organic species are detected; Bottinelli et al. 2004) and the outer envelope using single-dish telescopes, these observations can be extremely helpful to constrain the HDO/H₂O ratio in the outer part of the protostellar envelopes ($T < 100$ K). Indeed, the extended emission coming from the cold envelope cannot be probed with interferometers. Only two Class 0 sources were consequently studied for their cold HDO/H₂O ratios². It was determined to be between 3×10^{-3} and 1.5×10^{-2} in IRAS 16293-2422 by Coutens et al. (2012, 2013), and between 9×10^{-3} and 1.8×10^{-1} in NGC 1333 IRAS 2A by Liu et al. (2011). The fundamental HDO $1_{1,1}$ – $0_{0,0}$ transition at 894 GHz observed with *Herschel*/HIFI at high sensitivity provides particularly strong constraints on the outer HDO abundance. In IRAS 16293-2422, this line shows a specific line profile with a very deep absorption in addition to emission (Coutens et al. 2012). Combined with the observation of the other fundamental HDO $1_{0,1}$ – $0_{0,0}$ transition at 465 GHz with the JCMT, Coutens et al. (2012) showed that a cold water-rich absorbing layer surrounds this source. Without this layer, the deep absorbing components cannot be reproduced. Similar conclusions were obtained for the D₂O absorbing lines observed with *Herschel* (Vastel et al. 2010; Coutens et al. 2013). However, the origin of this absorbing layer is not clearly determined. It has been suggested, for example, that it could result from an equilibrium between photodesorption and photodissociation by the UV interstellar radiation field, as predicted by Hollenbach et al. (2009). It would thus be helpful to know if this layer is observed around other protostars. Indeed, the ubiquity of this layer would give clues to the nature of this layer.

A collaboration between three *Herschel* key programs: CHESS (Chemical *Herschel* Surveys of Star forming regions; Ceccarelli et al. 2010), WISH (Water In Star-forming regions with *Herschel*; van Dishoeck et al. 2011), and HEXOS (*Herschel*/HIFI observations of EXtraOrdinary Sources: The Orion and Sagittarius B2 Star-forming Regions; Bergin et al. 2010) was set up to investigate the water chemistry in star-forming regions. As part of this collaboration, new observations of HDO were carried out towards two low-mass protostars, IRAS 4A and IRAS 4B, allowing us to estimate the HDO abundance profiles in these sources. These results are useful to derive, in particular, the HDO/H₂O ratio in the outer envelope of these protostars. These two sources are located in the NGC 1333 reflection nebula in the Perseus molecular cloud. They are separated by $31''$ (~ 7500 AU), and IRAS 4A is a binary system with a separation of $\sim 1.8''$ between its two components (Lay et al. 1995; Jørgensen et al. 2007). These protostars are well known for the complex organic chemistry observed in their hot corinos (Bottinelli et al. 2004, 2007; Sakai et al. 2006; Persson et al. 2012) and for their outflows detected in particular in CO, SiO, and CS (see, e.g., Blake et al. 1995; Lefloch et al. 1998; Choi 2005; Yıldız et al. 2012) and in H₂O (Kristensen et al. 2010, 2012). The distance to the NGC 1333 region is uncertain (see Curtis et al. 2010 for more details). We adopt here the distance of 235 ± 18 pc determined by Hirota et al. (2008) using very-long-baseline interferometry (VLBI) parallax measurements of water masers in SVS 13 located in the same cloud.

² We call warm HDO/H₂O ratios the HDO/H₂O ratios measured in the warm gas of the protostellar envelope ($T \geq 100$ K). The cold HDO/H₂O ratios refer then to the measure in the cold gas of the outer envelope ($T < 100$ K).

Table 1. Parameters for the observed HDO lines.

Frequency (GHz)	$J_{Ka,Kc}$	E_{up}/k (K)	A_{ij} (s^{-1})	Telescope	Beam size ($''$)	F_{eff}	B_{eff}	rms ^a (mK)	$\int T_{mb} dv^b$ (K km s ⁻¹)
NGC 1333 IRAS 4A									
80.5783	1 _{1,0} –1 _{1,1}	47	1.32×10^{-6}	IRAM-30 m	31.2	0.95	0.78	4	0.025 ± 0.005
225.8967	3 _{1,2} –2 _{2,1}	168	1.32×10^{-5}	IRAM-30 m	11.1	0.91	0.54	9	0.26 ± 0.03
241.5616	2 _{1,1} –2 _{1,2}	95	1.19×10^{-5}	IRAM-30 m	10.4	0.90	0.57	18	0.25 ± 0.04
464.9245	1 _{0,1} –0 _{0,0}	22	1.69×10^{-4}	JCMT	10.8	–	0.44 ^c	53	1.8 ± 0.2^d
599.9267	2 _{1,1} –2 _{0,2}	95	3.45×10^{-3}	HIFI 1b	35.9	0.96	0.75	7	≤ 0.05
893.6387	1 _{1,1} –0 _{0,0}	43	8.35×10^{-3}	HIFI 3b	24.1	0.96	0.74	4	0.55 ± 0.02^d
Outflow position of NGC 1333 IRAS 4A									
599.9267	2 _{1,1} –2 _{0,2}	95	3.45×10^{-3}	HIFI 1b	35.9	0.96	0.75	7	≤ 0.05
893.6387	1 _{1,1} –0 _{0,0}	43	8.35×10^{-3}	HIFI 3b	24.1	0.96	0.74	4	0.27 ± 0.01^d
NGC 1333 IRAS 4B									
80.5783	1 _{1,0} –1 _{1,1}	47	1.32×10^{-6}	IRAM-30 m	31.2	0.95	0.81	4	0.031 ± 0.009
225.8967	3 _{1,2} –2 _{2,1}	168	1.32×10^{-5}	IRAM-30 m	11.1	0.91	0.61	9	≤ 0.05
241.5616	2 _{1,1} –2 _{1,2}	95	1.19×10^{-5}	IRAM-30 m	10.4	0.90	0.57	4	0.051 ± 0.008
464.9245	1 _{0,1} –0 _{0,0}	22	1.69×10^{-4}	APEX	13.4	0.95	0.60	40	1.2 ± 0.1^d
599.9267	2 _{1,1} –2 _{0,2}	95	3.45×10^{-3}	HIFI 1b	35.9	0.96	0.75	6	0.07 ± 0.01
893.6387	1 _{1,1} –0 _{0,0}	43	8.35×10^{-3}	HIFI 3b	24.1	0.96	0.74	4	0.40 ± 0.01^d

Notes. The frequencies, the upper state energies (E_{up}), and the Einstein coefficients (A_{ij}) of HDO come from the spectroscopic catalog JPL (Pickett et al. 1998). ^(a) The rms (in T_{mb}) is computed for a spectral resolution of 0.5 km s^{-1} . ^(b) The calibration uncertainties are not taken into account in the flux uncertainties. ^(c) This value corresponds to the ratio between the beam efficiency and the forward efficiency. ^(d) For these lines, the integrated intensity is directly estimated, combining both emission and absorption components. To derive the flux of the different components (broad and narrow emission components and absorption component), we refer to Table 2.

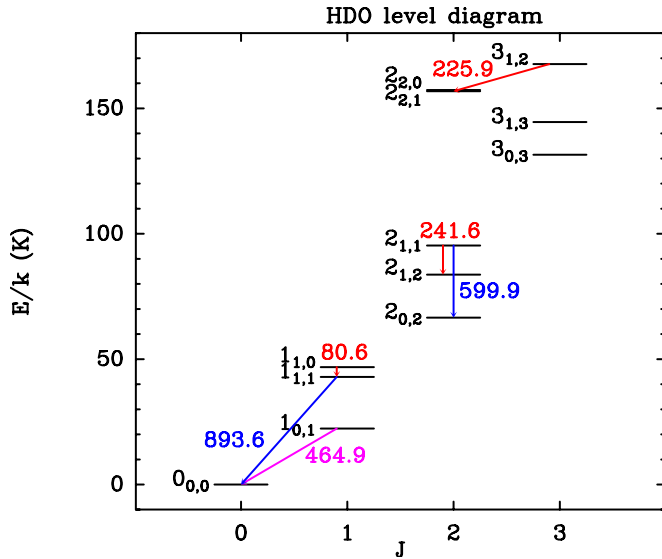


Fig. 1. Energy level diagram of the HDO lines. In red, IRAM-30 m observations; in magenta, JCMT/APEX observation; in blue, HIFI observations. The frequencies are written in GHz.

The paper is organized as follows. First, we present the observations in Sect. 2. Then we describe the modeling and show the results in Sect. 3. Finally, we discuss the results in Sect. 4 and conclude in Sect. 5.

2. Observations

The various transitions observed towards IRAS 4A and IRAS 4B are shown in the energy level diagram in Fig. 1 and summarized in Table 1. The original observations (without subtraction of the broad outflow component) of the $1_{1,1}$ –0_{0,0} and $1_{0,1}$ –0_{0,0}

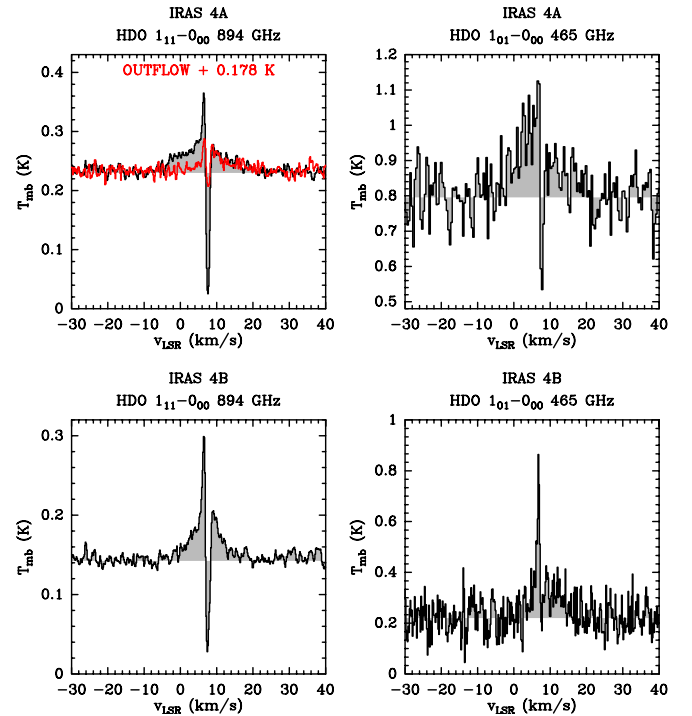


Fig. 2. Upper-left panel: HIFI observations of the fundamental line at 894 GHz towards the protostar IRAS 4A (black) and an outflow position (red, discussed in Sect. 3.3). The spectrum at the outflow position has been shifted vertically by 0.178 K. Upper-right panel: JCMT observations of the fundamental line at 465 GHz towards IRAS 4A. Lower-left panel: HIFI observations of the fundamental line at 894 GHz towards the protostar IRAS 4B. Lower-right panel: APEX observations of the fundamental line at 465 GHz towards IRAS 4B. The continuum refers to SSB data for each panel.

fundamental transitions are presented in Fig. 2. The other transitions are shown with the modeling in Figs. 5 and 7.

Table 2. HDO line components observed towards IRAS 4A and IRAS 4B.

		Broad emission component			Narrow emission component			Absorption component		
Frequency (GHz)	$J_{\text{Ka,Kc}}$	$T_{\text{mb}}^{\text{peak}}$ (K)	$FWHM$ (km s ⁻¹)	v_{LSR} (km s ⁻¹)	$T_{\text{mb}}^{\text{peak}}$ (K)	$FWHM$ (km s ⁻¹)	v_{LSR} (km s ⁻¹)	$T_{\text{mb}}^{\text{peak}}$ (K)	$FWHM$ (km s ⁻¹)	v_{LSR} (km s ⁻¹)
NGC 1333 IRAS 4A										
80.5783	1 _{1,0} –1 _{1,1}	–	–	–	0.013 ± 0.003	1.4 ± 0.4	5.8 ± 0.2	–	–	–
225.8967	3 _{1,2} –2 _{2,1}	–	–	–	0.032 ± 0.004	7.9 ± 0.9	6.0 ± 0.4	–	–	–
241.5616	2 _{1,1} –2 _{1,2}	–	–	–	0.047 ± 0.006	5.4 ± 0.9	7.9 ± 0.4	–	–	–
464.9245	1 _{0,1} –0 _{0,0}	0.12 ± 0.02	15.9 ^a	5.9 ^a	0.25 ± 0.05	1.8 ± 0.5	7.0 ± 0.3	–0.62 ± 0.07	0.9 ± 0.1	7.7 ± 0.1
893.6387	1 _{1,1} –0 _{0,0}	0.040 ± 0.002	15.9 ± 0.6	5.9 ± 0.2	0.14 ± 0.01	2.0 ± 0.1	7.2 ± 0.1	–0.38 ± 0.01	1.2 ± 0.1	7.6 ± 0.1
NGC 1333 IRAS 4B										
80.5783	1 _{1,0} –1 _{1,1}	–	–	–	0.006 ± 0.002	5 ± 2	8.2 ± 0.7	–	–	–
241.5616	2 _{1,1} –2 _{1,2}	–	–	–	0.014 ± 0.002	4.3 ± 0.8	6.9 ± 0.3	–	–	–
464.9245	1 _{0,1} –0 _{0,0}	0.08 ± 0.02	10.0 ^a	6.8 ^a	0.6 ± 0.4	1.1 ± 0.2	7.0 ± 0.4	–0.6 ± 0.6	0.7 ± 0.3	7.4 ± 0.1
599.9267	2 _{1,1} –2 _{0,2}	–	–	–	0.029 ± 0.003	2.7 ± 0.4	7.6 ± 0.2	–	–	–
893.6387	1 _{1,1} –0 _{0,0}	0.044 ± 0.003	10.0 ± 0.4	6.8 ± 0.2	0.22 ± 0.03	2.0 ± 0.1	7.4 ± 0.1	–0.39 ± 0.01	1.3 ± 0.1	7.6 ± 0.1

Notes. Obtained from Gaussian fits to each component using the Levenberg-Marquardt algorithm (Levenberg 1944; Marquardt 1963). The uncertainties are statistical and do not include the calibration uncertainties. ^(a) Fixed parameters.

2.1. HIFI data

In the framework of a collaboration between the CHESSE, WISH, and HEXOS *Herschel* key programs, two HDO transitions were observed with the HIFI instrument towards the solar-type protostars IRAS 4A and IRAS 4B: the fundamental 1_{1,1}–0_{0,0} line at 894 GHz with $E_{\text{up}} = 43$ K, and the 2_{1,1}–2_{0,2} line at 600 GHz with $E_{\text{up}} = 95$ K (see Table 1). The targeted coordinates are $\alpha_{2000} = 3^{\text{h}}29^{\text{m}}10^{\text{s}}.5$, $\delta_{2000} = 31^{\circ}13'30.9''$ for IRAS 4A, and $\alpha_{2000} = 3^{\text{h}}29^{\text{m}}12^{\text{s}}.0$, $\delta_{2000} = 31^{\circ}13'8.1''$ for IRAS 4B. The two transitions were also observed in the red-shifted part of the outflow emanating from IRAS 4A at $\alpha_{2000} = 3^{\text{h}}29^{\text{m}}10^{\text{s}}.8$, $\delta_{2000} = 31^{\circ}13'50.9''$. It corresponds to an offset position (+4'', +20'') with respect to IRAS 4A. This position was chosen using the map of the CO 6–5 line in Fig. 3 of Yıldız et al. (2012), so that the telescope half power beam width (HPBW) at 600 and 894 GHz (36 and 24'', respectively) do not include the position of the IRAS 4A source.

The pointed observations were obtained in August 2011, using the HIFI double beam switch (DBS) fast chop mode with optimization of the continuum. The DBS reference positions were situated at 3' from the source. We checked that no line was detected in the OFF-position spectra. The HIFI wide band spectrometer (WBS) was used, providing a spectral resolution of 1.1 MHz (0.55 km s⁻¹ at 600 GHz and 0.37 km s⁻¹ at 894 GHz). The data were processed using the standard HIFI pipeline up to frequency and amplitude calibrations (level 2) with the ESA-supported package HIPE 7.1 (Ott 2010). After being inspected separately, the H and V polarizations were averaged weighting them by the observed noise, using the GILDAS/CLASS³ software. The forward efficiency is about 0.96 and the main beam efficiency about 0.74–0.75 (Roelfsema et al. 2012). The HIFI instrument uses double sideband receivers. A sideband gain ratio of 1 is assumed to estimate the continuum value at 894 GHz (Roelfsema et al. 2012), necessary in the modeling of the deep absorption line. The continuum was fitted with a polynomial of degree 1. Standing waves are not visible in the observations. From Roelfsema et al. (2012), we thus estimate the uncertainties on the continuum level to be less than 10% for both IRAS 4A and IRAS 4B observations. Observations were also carried out with the high resolution spectrometer (HRS). The WBS and HRS observations are in agreement (see Fig. A.1).

³ <http://www.iram.fr/IRAMFR/GILDAS/>

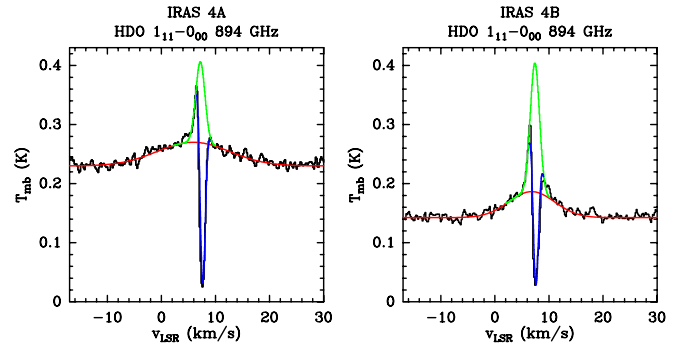


Fig. 3. Decomposition of the 1_{1,1}–0_{0,0} fundamental transitions observed towards IRAS 4A and IRAS 4B with HIFI in three Gaussians: a broad emission component (red), a narrower emission component (green), and a narrow absorption component (blue). The parameters of the Gaussian fits are given in Table 2.

The line profiles observed at 894 GHz clearly show a broad emission component tracing the outflows, a narrower emission component tracing the envelope, and a deep narrow absorption component (see Fig. 3). The parameters of the three components, fitted by Gaussians using the CASSIS⁴ software, are presented in Table 2. Figure 2 superposes the HIFI HDO spectra towards IRAS 4A and the position in the red outflow lobe. The spectrum in the red lobe is similar to that towards IRAS 4A except that the blue outflow wing is no longer seen. The absorption appears less deep because of the lower continuum level at the outflow position.

2.2. JCMT data

The HDO 1_{0,1}–0_{0,0} fundamental transition at 465 GHz (Table 1) was observed towards the source IRAS 4A with the JCMT in September 2004 (project M04BN06). The spectral resolution of the observations is 0.1 km s⁻¹. As in the case of the other fundamental transition at 894 GHz observed with HIFI, three components are observed: a broad component tracing the outflows, a narrower emission line, and a deep absorption component (see Fig. 2). The continuum level is ~0.8 K with an

⁴ CASSIS (<http://cassis.irap.omp.eu>) has been developed by IRAP-UPS/CNRS.

uncertainty of 13% obtained from the comparison of the spectra in the dataset. The full width at half maximum (FWHM) and the peak-intensity velocity of the Gaussian fitted on the broad component at 894 GHz are consistent with the data at 465 GHz. The fit results from the higher signal-to-noise ratio profile at 894 GHz were then fixed for the 465 GHz profile to determine the intensity of the broad component (see Table 2). Keeping parameters free would not affect the results significantly.

2.3. APEX data

The HDO $1_{0,1}-0_{0,0}$ fundamental transition was also observed towards IRAS 4B with the Swedish Heterodyne Facility Instrument (SHeFI) receiver at 460 GHz of the APEX telescope. The observations were carried out in October 2012 using the wobbler symmetric switching mode with an amplitude of 150'', resulting in OFF positions at 300'' from the source. The beam efficiency and the forward efficiency are shown in Table 1. This fundamental line again shows a broad emission component, a narrow emission component, and a weak absorbing component. The absorbing component appears weaker than in IRAS 4A, because the absorbing line is slightly shifted with respect to the velocity of the narrower emission component, leading to less absorption than there would be if the velocity of the absorption was exactly the same as the velocity of the emission. A continuum level cannot be extracted with precision from these observations. It is estimated at about 0.2 K according to the model predictions (see Sect. 3.2). The continuum level would then be lower in IRAS 4B than in IRAS 4A (~ 0.8 K), which also implies a shallower absorption in IRAS 4B for the same column density of the absorber.

2.4. IRAM data

Three additional transitions at 81 ($1_{1,0}-1_{1,1}$), 226 ($3_{1,2}-2_{2,1}$), and 242 GHz ($2_{1,1}-2_{1,2}$) were observed with the IRAM-30 m telescope towards IRAS 4A. The observations were carried out in November 2004 for the 81 and 226 GHz lines with the VESPA autocorrelator in wobbler switching mode, whereas the 242 GHz transition was observed in April 2012 in position switching mode using the fast Fourier transform spectrometer (FTS) at a 200 kHz resolution. The spectral resolution is 0.14, 0.10, and 0.24 km s⁻¹ for the 81, 226, and 242 GHz transitions respectively. For clarity, the spectra shown hereafter were smoothed to a resolution of $\sim 0.4-0.6$ km s⁻¹.

These three transitions were also observed towards IRAS 4B in January 2013. The observations were carried out in position switching mode using the FTS with a fine spectral resolution of 50 kHz. The beam efficiencies and forward efficiencies for the different observations are shown in Table 1.

Table 2 summarizes, for each line, the Gaussian parameters of the different components derived with CASSIS. The FWHM of the narrower emission component is different depending on the line. Indeed these sources undergo an infall which necessarily leads to higher FWHM for the excited lines, such as the $3_{1,2}-2_{2,1}$ and $2_{1,1}-2_{1,2}$ transitions that probe the warm inner regions, and smaller FWHM for the fundamental lines that probe a colder medium. Moreover, the determination of the FWHM for the fundamental lines could be underestimated because of the blending between the narrow emission and absorption components. Only the broad emission component can be clearly extracted thanks to the absence of blending at high velocities ($\Delta v > 3$ km s⁻¹).

3. Modeling and results

3.1. Protostellar envelope of NGC 1333 IRAS 4A

The spherical non-LTE (local thermal equilibrium) radiative transfer code RATRAN (Hogerheijde & van der Tak 2000), which includes continuum emission and absorption by dust, was used to determine the HDO abundances in the protostellar envelope. First, it was necessary to subtract the broad outflow component fitted by a Gaussian profile (see Table 2) from the HDO fundamental transitions at 465 and 894 GHz. Then a similar method to the study on the protostar IRAS 16293-2422 (Coutens et al. 2012) was carried out on the line profiles obtained after the removal of the broad component. We used the HDO collisional rates calculated with ortho and para-H₂ (Faure et al. 2011; Wiesenfeld et al. 2011), assuming an ortho/para ratio of H₂ at local thermodynamic equilibrium with the gas temperature. The density and temperature radial profiles of the source IRAS 4A were determined by Kristensen et al. (2012). The envelope mass is estimated at 5.2 M_{\odot} (Kristensen et al. 2012), and the radius of the protostellar envelope extends from 33.5 AU to 33 500 AU. The density power-law index is 1.8. At $r = 1000$ AU, the density is equal to 6.7×10^6 cm⁻³, and the temperature is 21 K. However, at small scale (≤ 500 AU, Jørgensen et al. 2004), the structure is rather uncertain because of the limited spatial resolution of the continuum maps used to determine the profiles. The velocity profile is assumed as a free-fall profile ($v = \sqrt{2GM/r}$). The central mass M was estimated at $\sim 0.5 M_{\odot}$ by Maret et al. (2002) and Jørgensen et al. (2009) and at $\sim 0.7 M_{\odot}$ by Di Francesco et al. (2001) and Mottram et al. (2013). Several grids of models with different values of M (0.3, 0.5, and 0.7 M_{\odot}) were then run. To reproduce the absorption component seen in the fundamental lines, the Doppler b-parameter (db), which is related to the turbulence broadening, is estimated at 0.4 km s⁻¹. This is the same as found independently for H₂O by Mottram et al. (2013). It means that the FWHM produced by the turbulence is equal to $db/0.6$, i.e., about 0.67 km s⁻¹. The continuum is not correctly fitted with the dust opacity used by Kristensen et al. (2012, model OH5 in Ossenkopf & Henning 1994). It is 17% lower than the observed continuum at 465 GHz and 28% higher at 895 GHz. Calibration uncertainties could play a role. The study of the absorbing components requires, however, the use of the correct continuum value. A power-law emissivity model was then estimated locally to fit the observed continuum,

$$\kappa = 8.5 \left(\frac{\nu}{10^{12}} \right)^{1.05}, \quad (1)$$

with κ the absorption coefficient in cm² g_{dust}⁻¹ and ν the frequency in Hz. We assumed an abundance profile with a jump at 100 K ($\theta \sim 0.73''$, $r \sim 85$ AU), for the release by thermal desorption of the water molecules trapped in the icy grain mantles into the gas phase (Fraser et al. 2001). This type of jump abundance profile was assumed in a number of studies of water and deuterated water in low-mass protostars (Ceccarelli et al. 2000; Parise et al. 2005; Liu et al. 2011; Coutens et al. 2012). A recent study shows, however, that in the outer envelope of low-mass protostars the H₂¹⁶O line profiles are better reproduced with an abundance increasing gradually with radius (Mottram et al. 2013). To compare the HDO abundances in IRAS 4A with previous results in other low-mass protostars and to keep a reasonable number of free parameters in the modeling, we used a jump abundance profile with a constant outer abundance for this study.

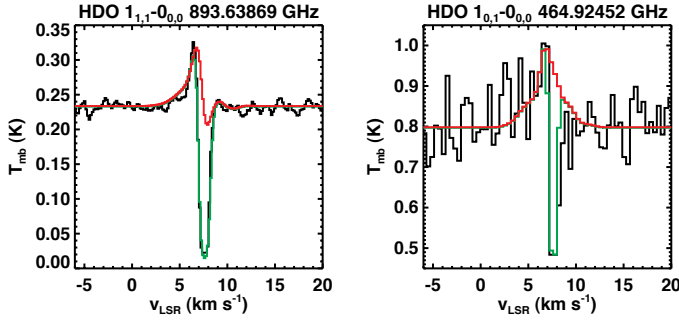


Fig. 4. Comparison of the modeling of the HDO $1_{1,1}-0_{0,0}$ and $1_{0,1}-0_{0,0}$ fundamental transitions observed towards IRAS 4A with an added absorbing layer (in green) and without this layer (in red). The HDO column density in the absorbing layer is about $1.4 \times 10^{13} \text{ cm}^{-2}$. The broad outflow component seen in the observations was subtracted. The continuum refers to SSB data.

Grids of models with different inner (X_{in}) and outer (X_{out}) abundances⁵, and central masses (M) were run. Similarly to IRAS 16293-2422 (Coutens et al. 2012), an absorbing layer had to be added to the structure to reproduce the absorption lines observed at 894 and 465 GHz, without overpredicting the line emissions. Figure 4 shows the difference of the modeling with and without the absorbing layer for an HDO column density of $1.4 \times 10^{13} \text{ cm}^{-2}$. The analysis and the discussion regarding this layer are detailed in Sect. 3.3. A χ^2 minimization was then used to determine the best-fit parameters, adding this absorbing layer to the structure. The χ^2 is computed on the line profiles with the formalism,

$$\chi^2 = \sum_{i=1}^N \sum_{j=1}^{n_{\text{chan}}} \frac{(T_{\text{obs},ij} - T_{\text{mod},ij})^2}{\text{rms}_i^2}, \quad (2)$$

with N the number of observed lines i , n_{chan} the number of channels j for each line, $T_{\text{obs},ij}$ and $T_{\text{mod},ij}$ the intensity observed and predicted by the model in the channel j of the line i , and rms_i the rms of the line i . Taking into account this foreground absorbing layer in the modeling, the best-fit is obtained for an inner abundance $X_{\text{in}} = 7.5 \times 10^{-9}$, an outer abundance $X_{\text{out}} = 1.2 \times 10^{-11}$, and a central mass $M = 0.5 M_{\odot}$. The line profiles predicted by this model are shown in Fig. 5, and the χ^2 contours at 1, 2, and 3σ are plotted in Fig. 6. At 3σ , the inner abundance is between 4.5×10^{-9} and 1.1×10^{-8} , whereas the outer abundance is between 8×10^{-12} and 1.6×10^{-11} . Although the models with $M = 0.3 M_{\odot}$ and $M = 0.7 M_{\odot}$ show higher χ^2 values, some of them are, however, included in the 3σ uncertainties. For these masses, the best-fit abundances remain quite similar: $X_{\text{in}} = 7.0 \times 10^{-9}$, $X_{\text{out}} = 1.2 \times 10^{-11}$ for $M = 0.3 M_{\odot}$ and $X_{\text{in}} = 8.5 \times 10^{-9}$, $X_{\text{out}} = 1.0 \times 10^{-11}$ for $M = 0.7 M_{\odot}$.

3.2. Protostellar envelope of NGC 1333 IRAS 4B

A similar modeling was carried out to determine the HDO abundance distribution in IRAS 4B. The outflow components were subtracted here again. We used the source structure determined by Kristensen et al. (2012), for which the radius of the protostellar envelope ranges between 15 AU and 12 000 AU and the envelope mass is about $3.0 M_{\odot}$. The density power-law index is 1.4. At $r = 1000$ AU, the density is $5.7 \times 10^6 \text{ cm}^{-3}$, and the

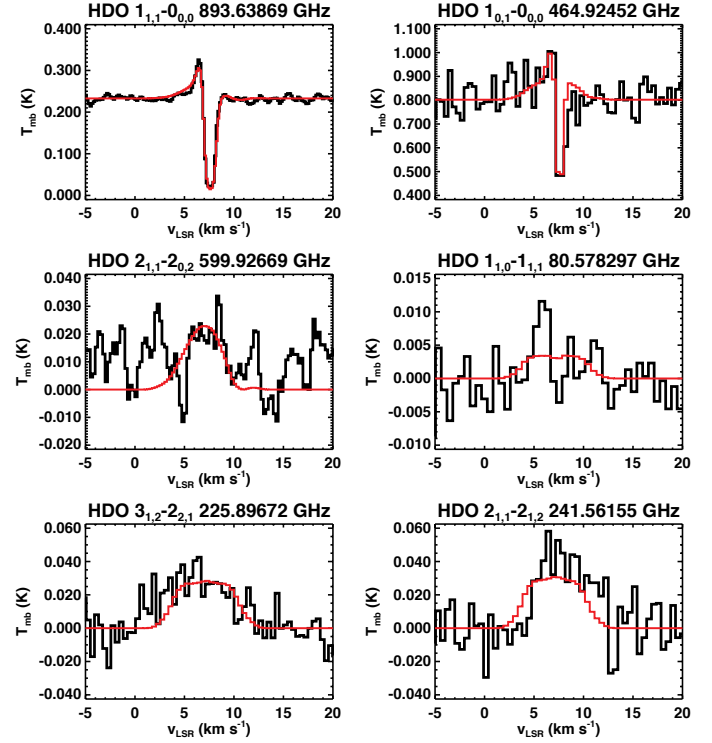


Fig. 5. In black: HDO lines observed towards IRAS 4A with HIFI, IRAM, and JCMT. The broad outflow component seen in the observations was subtracted. The continuum seen in the observations of the 894 GHz and 465 GHz lines refers to SSB data. In red: best-fit model obtained when adding an absorbing layer with an HDO column density of $\sim 1.4 \times 10^{13} \text{ cm}^{-2}$ to the structure. The best-fit inner abundance is 7.5×10^{-9} and the best-fit outer abundance is 1.2×10^{-11} .

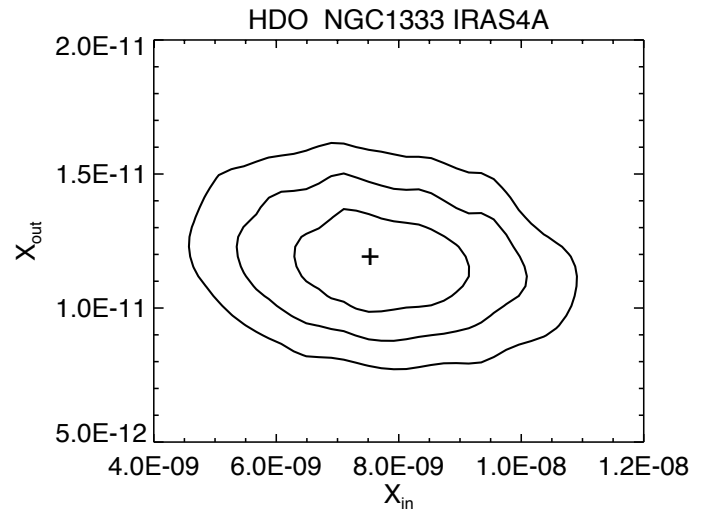


Fig. 6. χ^2 contours at 1σ , 2σ , and 3σ obtained for IRAS 4A when adding an absorbing layer with an HDO column density of $1.4 \times 10^{13} \text{ cm}^{-2}$ to the structure. The best-fit model is represented by the symbol “+”. The mass is equal to $0.5 M_{\odot}$.

temperature is 17 K. As in the case of IRAS 4A, the structure is quite uncertain at small scale. According to this structure, the size of the abundance jump ($T > 100$ K) is $\theta \sim 0.4''$, i.e., $r \sim 47$ AU. When the absorbing layer defined for IRAS 4A ($N(\text{HDO}) = 1.4 \times 10^{13} \text{ cm}^{-2}$) is added to the structure of its nearby companion IRAS 4B, the absorbing components are well reproduced (see Fig. 7). The velocity profile is assumed to be a

⁵ The HDO abundances quoted in the paper correspond to the $N(\text{HDO})/N(\text{H}_2)$ ratio.

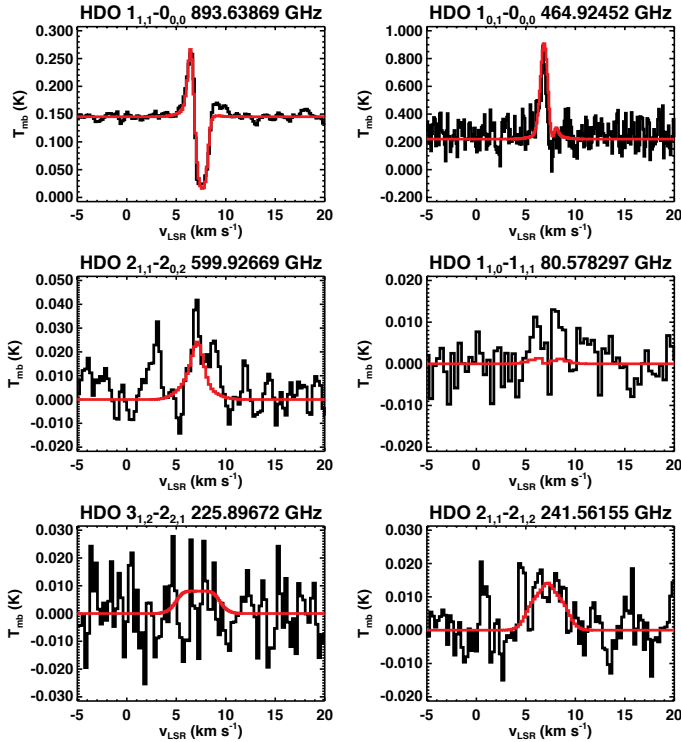


Fig. 7. In *black*: HDO lines observed towards IRAS 4B with HIFI, IRAM, and APEX. The broad outflow component seen in the observations was subtracted. The continuum seen in the observations of the 894 GHz and 465 GHz lines refers to SSB data. In *red*: best-fit model obtained when adding the absorbing layer used to model the IRAS 4A lines ($N(\text{HDO}) \sim 1.4 \times 10^{13} \text{ cm}^{-2}$). The best-fit inner abundance is 1×10^{-8} and the best-fit outer abundance is 1.2×10^{-10} .

free-fall profile. The central mass M derived in previous studies varies by more than a factor of 2. Di Francesco et al. (2001) and Jørgensen et al. (2009) predicted a mass about $0.2 M_{\odot}$, whereas Maret et al. (2002) determined a mass about $0.5 M_{\odot}$.

Several values were then considered for the central mass M chosen from $0.1 M_{\odot}$ to $0.5 M_{\odot}$ in steps of $0.1 M_{\odot}$. The Doppler b-parameter is estimated at 0.5 km s^{-1} , to reproduce the deep absorbing component at 894 GHz. We used the emissivity model determined by Ossenkopf & Henning (1994), for thin ice-coated grains with a growth of 10^6 years (OH5, similar to Kristensen et al. 2012), which gives a dust continuum value in agreement with the *Herschel*/HIFI observations. The continuum level at 465 GHz is then predicted at about 0.2 K for the APEX beam.

Running a grid with different values for X_{in} , X_{out} , and M , the best-fit model is obtained for an inner abundance of about 1×10^{-8} , an outer abundance of about 1.2×10^{-10} , and a central mass of about $0.1 M_{\odot}$. The best-fit line profiles are overplotted on the observations in Fig. 7. The χ^2 contours are shown in Fig. 8. At 3σ , the inner abundance varies between 1.5×10^{-9} and 2.8×10^{-8} , whereas the outer abundance is included between 8.5×10^{-11} and 1.75×10^{-10} . Some models with $M = 0.2 M_{\odot}$ are also included in the 3σ uncertainties, but not for masses higher than or equal to $0.3 M_{\odot}$.

3.3. Absorbing layer

Depending on the position of the absorbing layer with respect to the outflows, the depth of the absorption components may vary after the subtraction of the broad component. Indeed, if the absorbing layer is situated between the outflows and the

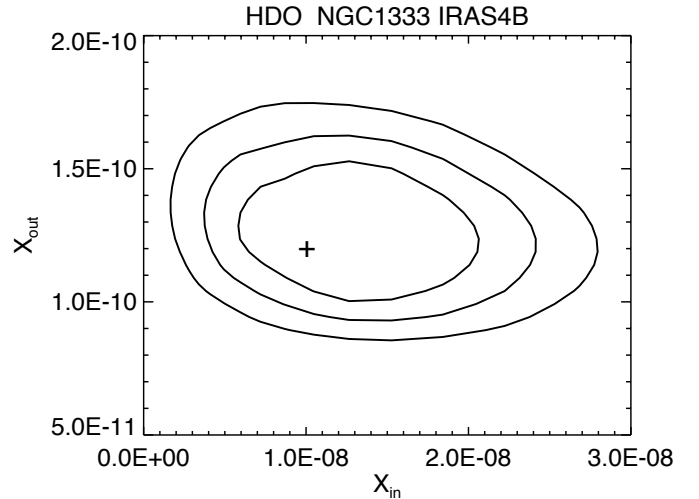


Fig. 8. χ^2 contours at 1σ , 2σ , and 3σ obtained for IRAS 4B when adding the absorbing layer used to model the IRAS 4A lines. The best-fit model is represented by the symbol “+”. The mass is equal to $0.1 M_{\odot}$.

protostellar envelope (see case (a) in Fig. 9), the depth of the absorption line has to be unchanged after the subtraction of the large component, because the continuum produced by the outflows (i.e., the broad component) is not absorbed by the added layer. On the contrary, if the absorbing layer is located in front of the outflows (see case (b) in Fig. 9), the continuum obtained after subtraction is lower than the real absorbed continuum, since the line wing effectively contributes to the continuum that is being absorbed. In this case, to accurately estimate the HDO column density in the absorbing layer, the depths of the absorbing lines must be corrected, reducing them by a value close to the intensities of the broad components. The uncertainty on this value is $\lesssim 10\%$, which is comparable to the calibration uncertainties of the HIFI observations and is probably even lower for the JCMT observations. The presence of an absorption component in the data at 894 GHz towards the outflow of IRAS 4A (see Fig. 2) suggests that the foreground absorbing layer is more extended than a part of the outflows (case (b) in Fig. 9). When subtracting the broad components on the IRAS 4A observations, the depth of the absorbing lines was consequently reduced to take into account the absorption by the continuum produced by the outflows. We assumed a similar behavior for IRAS 4B and treated the absorptions in the same way.

To reproduce the depth of the absorption lines, the column density of HDO is then about $1.4 \times 10^{13} \text{ cm}^{-2}$. The temperature is assumed to be between 10 and 30 K and the H_2 density is found to be lower than 10^5 cm^{-3} to reproduce the absorptions. This upper limit on the H_2 density is consistent with the study by Coutens et al. (2013) using the D_2O lines observed towards IRAS 16293-2422. The HDO column density derived here differs by less than a factor of 2 compared with the estimate in the absorbing layer of IRAS 16293-2422 ($2.3 \times 10^{13} \text{ cm}^{-2}$; Coutens et al. 2012). As the absorbing layer shows the same characteristics for IRAS 4A and IRAS 4B, this could mean that this layer is sufficiently extended ($\gtrsim 7000 \text{ AU}$) to encompass the two sources.

Several molecules (CO , HCN , HCO^+ , H_2CO) show, over a large extent ($\gtrsim 200''$) around IRAS 4, asymmetric line-profiles with dips at a velocity about 8 km s^{-1} ($\sim 7.5 \text{ km s}^{-1}$ at the IRAS 4A position; Choi et al. 2004). In our data, the velocity of the absorbing components appears at 7.6 km s^{-1} . These molecules and water could consequently arise from the same absorbing layer. The origin of this absorbing layer was largely

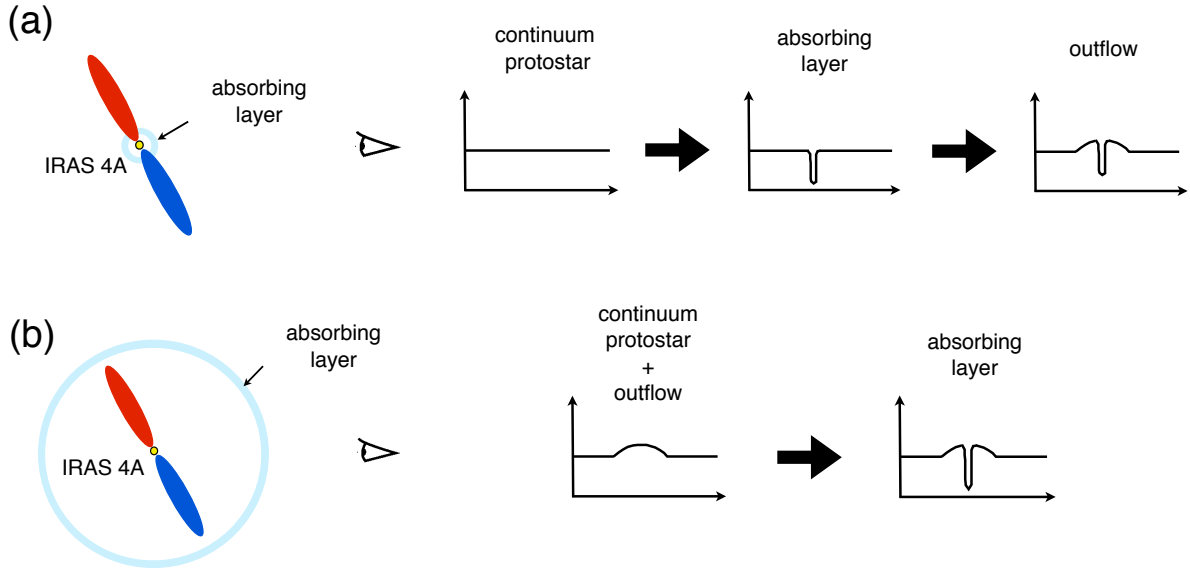


Fig. 9. Different scenarios for the position of the absorbing layer with respect to the protostar and the outflows and influence on the absorbing line depth. In case **a)**, the absorbing layer is less extended than the outflows. The continuum that is absorbed is only due to the protostar. The broad component is superposed. In case **b)**, the absorbing layer is more extended than the outflows. The continuum that is absorbed is due both to the protostar and the outflows.

debated (e.g., Langer et al. 1996; Di Francesco et al. 2001; Choi 2001, and references therein). In particular, Choi et al. (2004) interpreted these absorptions as produced by a cold foreground layer unrelated to the IRAS 4A source. This interpretation was, however, questioned by Belloche et al. (2006), as they showed that an infall motion would be sufficient to explain the observed absorptions of CS and N_2H^+ transitions if a source velocity of 7.2 km s^{-1} is assumed instead of the value of 6.7 km s^{-1} used by Choi et al. (2004). Walsh et al. (2006) drew similar conclusions, favoring the interpretation that the HCO^+ line profiles are indicative of large-scale inward motions associated with the IRAS4A source. In our study, nothing allows us to conclude that the water-rich absorbing layer is unrelated to the protostellar sources. This cold layer could consequently be a part of the complex surrounding IRAS 4.

While it is not surprising to detect molecules such as CO, HCO^+ , etc., in cold environments, the presence of water is more puzzling. Indeed, at low temperatures, water is mainly trapped on the grain mantles. Hypotheses were suggested by Coutens et al. (2012) to explain the presence of a water-rich absorbing layer surrounding the protostar IRAS 16293-2422. The most probable explanation is that this layer results from an equilibrium between the photodesorption of water molecules trapped in the icy grain mantles and their photodissociation by an external UV radiation field, as predicted by Hollenbach et al. (2009) in molecular clouds at a visual extinction A_V between 1 and 4. Assuming the relation $N_H/A_V = 2 \times 10^{21} \text{ cm}^{-2} \text{ mag}^{-1}$ (Vuong et al. 2003), the deuterated water abundance with respect to H_2 would then be $\sim 3.7 \times 10^{-9}$ – 1.5×10^{-8} in the assumed photodesorption layer of IRAS 4, which is comparable to the layer surrounding IRAS 16293-2422 ($\sim 6 \times 10^{-9}$ – 2.4×10^{-8}). Other mechanisms able to explain the presence of gaseous water in a cold layer are discussed in Appendix B.

We have to point out that photodesorption by the cosmic-ray induced UV-field certainly plays a role in the outer envelope, as shown by Mottram et al. (2013) in low-mass protostars and Caselli et al. (2012) in prestellar cores. In this case, the abundance increases gradually with the outer radius. As the outer

abundance is assumed to be constant here, a part of the absorption could also be produced in the outermost part of the envelope (which encompasses the outflow position and shows low temperatures as well as low densities). The column density of water derived in the added absorbing layer should then be considered to be an upper limit. An analysis of the HDO lines with a more physical abundance profile in the outer layer would be required to know the proportion of cold water in the outer envelope and at larger scale in the molecular cloud.

3.4. Outflow of NGC 1333 IRAS 4A

A broad component tracing the outflows is seen in the two fundamental $1_{1,1}-0_{0,0}$ and $1_{0,1}-0_{0,0}$ transitions observed with HIFI and JCMT towards IRAS 4A. This HDO outflow component is very similar to the broad component seen on the CO 6–5 line profile observed with APEX by Yıldız et al. (2012) (see Fig. 10), suggesting a common origin for the entrainment of the HDO and CO molecules. The RADEX non-LTE radiative transfer code (van der Tak et al. 2007) was employed to estimate the HDO column density present in the outflows of IRAS 4A. We used a H_2 density of $3 \times 10^5 \text{ cm}^{-3}$ and a temperature between 100 and 150 K, as determined by Yıldız et al. (2012) for CO in the outflow positions R1 and B1. The HDO column density is estimated at $\sim (2-4) \times 10^{13} \text{ cm}^{-2}$. These estimates remain valid, even if the temperature is lower than 100 K. Using the H_2 column density of $(2.1-2.8) \times 10^{22} \text{ cm}^{-2}$ estimated by Yıldız et al. (2012) in the outflows, the HDO abundance is therefore about 7×10^{-10} – 1.9×10^{-9} .

The HDO/ H_2O ratio in the outflows can be also estimated with RADEX using the line ratios of the HDO $1_{1,1}-0_{0,0}$ line at 894 GHz with the para- H_2O $1_{1,1}-0_{0,0}$ line at 1113 GHz (Kristensen et al. 2010). At these frequencies, the beam sizes are quite similar ($19''$ vs. $24''$). An ortho-to-para ratio of 3 is assumed to consider the H_2O abundance. The profile of the para- H_2O line appears quite different from that of the HDO line (see Fig. 10). The H_2O outflow profile shows a peak intensity

Table 3. HDO abundances with respect to H₂ determined in several low-mass star-forming regions.

Source	Inner abundance ^a	Outer abundance ^a	Absorbing layer N(HDO) (cm ⁻²)	Outflow abundance	References
NGC 1333 IRAS 4A	$7.5^{+3.5}_{-3.0} \times 10^{-9}$	$1.2^{+0.4}_{-0.4} \times 10^{-11}$	1.4×10^{13}	$0.7\text{--}1.9 \times 10^{-9}$	This paper
NGC 1333 IRAS 4B	$1.0^{+1.8}_{-0.9} \times 10^{-8}$	$1.2^{+0.6}_{-0.4} \times 10^{-10}$	1.4×10^{13}	–	This paper
NGC 1333 IRAS 2A	$8^{+2.0}_{-1.2} \times 10^{-8}$	$7^{+11}_{-6.1} \times 10^{-10}$	–	–	Liu et al. (2011)
IRAS 16293-2422	$1.8^{+0.6}_{-0.4} \times 10^{-7}$	$8^{+2.0}_{-3.4} \times 10^{-11}$	2.3×10^{13}	–	Coutens et al. (2012, 2013)
L1448-mm	4×10^{-7}	–	–	–	Codella et al. (2010)

Notes. ^(a) The uncertainties correspond to the 3σ confidence interval.

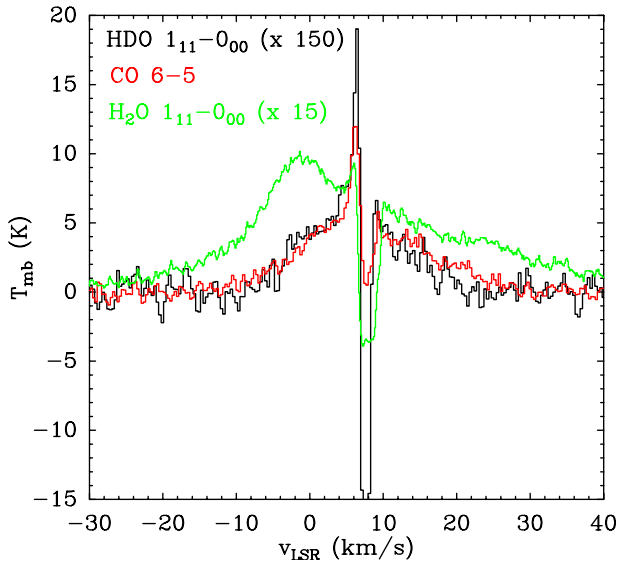


Fig. 10. Comparison of the line profiles of the CO 6–5 transition (in red), the HDO $1_{1,1}\text{--}0_{0,0}$ transition (in black, intensities multiplied by 150), and the H₂O $1_{1,1}\text{--}0_{0,0}$ transition (in green, intensities multiplied by 15) towards IRAS 4A.

at -0.6 km s^{-1} that we do not see for the HDO lines. Kristensen et al. (2010) fitted it with a sum of two Gaussians, one centered at -0.6 km s^{-1} and a broader one centered at 8.7 km s^{-1} . However, it is not possible to reproduce the HDO profile with the same velocity and FWHM. To estimate the HDO/H₂O abundance ratio in the outflows, we consequently compared the predicted line ratios with the line ratios at the velocities where the HDO broad component is detected. A range of densities ($10^5\text{--}10^7 \text{ cm}^{-3}$) and temperatures (100–1000 K) was considered. The derived HDO/H₂O ratio ranges between 1×10^{-3} and 9×10^{-2} in the red part of the outflow and between 7×10^{-4} and 6×10^{-2} in the blue part of the outflow. These estimates are consistent with the HDO/H₂O ratio derived by Taquet et al. (2013a) in the hot corino of IRAS 4A ($5 \times 10^{-3}\text{--}3 \times 10^{-2}$). If the HDO/H₂O ratios are actually similar in the outflow and in the hot corino, it could mean that water is contained in grain mantles and then released into the gas phase by sputtering in outflows and thermal desorption in the warm inner envelope. The isotopologue HDO would then be omnipresent and produced early in the evolution of the core. However, the wide range of values determined here does not allow us to clearly assert this possibility. The HDO/H₂O ratio is not determined at high velocities ($\Delta v > 10 \text{ km s}^{-1}$) where only H₂O is detected.

4. Discussion

4.1. Comparison of the HDO abundances in low-mass star-forming regions

Table 3 summarizes the HDO abundances measured in low-mass protostars. For all sources except L1448-mm, the derived abundances are based on RATRAN modeling of multi-line single-dish observations. For IRAS 16293-2422, IRAS 4A, and IRAS 4B, the HDO fundamental $1_{1,1}\text{--}0_{0,0}$ transition was observed at high sensitivity with *Herschel*/HIFI, allowing us to strongly constrain the outer abundance of deuterated water. The estimate of the HDO inner abundance in L1448-mm by Codella et al. (2010) is based on interferometric observations of the HDO $1_{1,0}\text{--}1_{1,1}$ line at 80.6 GHz. Using the spherical source structure determined by Jørgensen et al. (2002), the abundance is then estimated at 4×10^{-7} . The source IRAS 4A shows the lowest HDO abundances among the low-mass protostars (both inner and outer), whereas IRAS 16293-2422 shows the highest inner abundance and IRAS 2A the highest outer abundance. The HDO outer abundances do not cover a wide range of values. They only range between $\sim 1 \times 10^{-11}$ and a few 10^{-10} . In addition, the HDO outer abundance of IRAS 2A ($\sim 7 \times 10^{-10}$) is not as strongly constrained as in the other sources, because the modeling did not include the HDO line observed with HIFI at 894 GHz. At 3σ , the HDO abundance could be as low as 9×10^{-11} in the colder envelope.

We searched for a correlation between the HDO abundances and different source parameters such as the submillimeter luminosity L_{smm} (i.e., measured longward of $350 \mu\text{m}$), the bolometric luminosity L_{bol} , and the bolometric temperature T_{bol} . Figure 11 shows the inner and outer abundances as a function of these parameters as well as the $L_{\text{smm}}/L_{\text{bol}}$ and $L_{\text{bol}}^{0.6}/M_{\text{env}}$ ratios (where M_{env} is the envelope mass). The $L_{\text{smm}}/L_{\text{bol}}$ ratio is an indicator of the evolution stage of star formation (André et al. 1993). The higher it is, the less evolved the protostar is. The function $L_{\text{bol}}^{0.6}/M_{\text{env}}$ is also considered to be correlated with the protostellar evolution (Bontemps et al. 1996). The bolometric temperature is a third parameter used to evaluate the evolutionary stage of the protostar (Myers & Ladd 1993), a higher bolometric temperature meaning that the source is more evolved. We do not find correlations of the abundances with the evolution of the protostars, L_{smm} or L_{bol} ; however we have to be careful with the estimate of the inner abundances. They are derived using the density profile estimated at large scale. The structure is consequently not constrained at scales comparable to the hot corino size. In addition, it seems that disks could already be present at the Class 0 stage (see for example Pineda et al. 2012). The ratio between the inner and outer abundances, also plotted in Fig. 11, could be correlated with the submillimeter luminosity which is physically

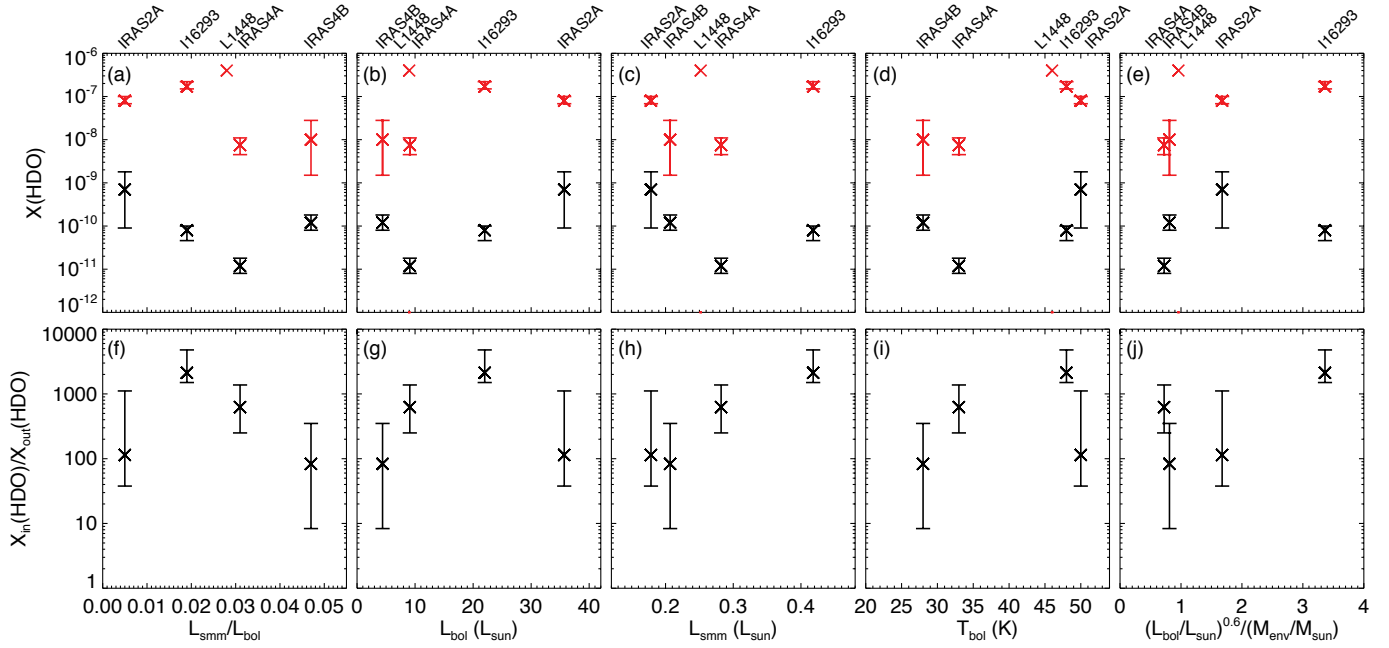


Fig. 11. Upper panels: comparison of the inner (red) and outer (black) HDO abundances estimated in the low-mass protostars IRAS 16293-2422, NGC 1333 IRAS 4A, NGC 1333 IRAS 2A, and L1448-mm (see also Table 3) as a function of **a)** the ratio between the submillimeter and bolometric luminosities $L_{\text{submm}}/L_{\text{bol}}$; **b)** the bolometric luminosity L_{bol} ; **c)** the submillimeter luminosity L_{submm} ; **d)** the bolometric temperature T_{bol} ; **e)** the ratio $L_{\text{bol}}^{0.6}/M_{\text{env}}$. Lower panels: comparison of the ratio between the inner and outer HDO abundances $X_{\text{in}}/X_{\text{out}}$ as a function of **f)** the $L_{\text{submm}}/L_{\text{bol}}$ ratio; **g)** L_{bol} ; **h)** L_{submm} ; **i)** T_{bol} ; **j)** $L_{\text{bol}}^{0.6}/M_{\text{env}}$. The different values of the parameters ($L_{\text{submm}}/L_{\text{bol}}$, L_{bol} , L_{submm} , T_{bol} , and M_{env}) come from Kristensen et al. (2012), Karska et al. (2013), Evans et al. (2009), Froebrich (2005), and Crimier et al. (2010). The HDO abundance is only estimated in the inner part of the protostellar envelope of L1448-mm using interferometric data (Codella et al. 2010). No uncertainty is provided for this value.

related to the envelope mass. However, it is not clear why this would happen. This correlation could be simply fortuitous. The low number of studies taken into account does not allow us to assert it at the moment.

Another point to check is the variation of the HDO abundances with the physical environment. Indeed the HDO abundances could also depend on the initial conditions of the molecular cloud in which they are embedded. In this case, it would be sensible to only compare the results for the sources situated in the NGC 1333 complex. A correlation between the HDO outer abundances and the submillimeter luminosities of the three NGC 1333 sources is then observed. The lower the L_{submm} parameter, the higher the outer abundance, which could simply reflect the fact that water trapped in the icy grain mantles is more efficiently released in the gas phase by non-thermal desorption mechanisms when the density is less important (i.e., when L_{submm} is low). Cosmic rays and UV photons could then penetrate more deeply in the envelope to desorb water molecules. It is also possible that it favors the ion-molecule reactions in the gas phase. This hypothesis is strengthened by the comparison of the outer abundance with the value of the density at 1000 AU (1.5×10^6 , 5.7×10^6 , and $6.7 \times 10^6 \text{ cm}^{-3}$ for IRAS 2A, IRAS 4B, and IRAS 4A, respectively), as X_{out} increases with decreasing H_2 densities. Therefore, the difference between the submillimeter luminosities of IRAS 4A and IRAS 4B could explain why the outer abundance is higher in IRAS 4B.

4.2. Water deuterium fractionation

4.2.1. Warm inner HDO/ H_2O ratios

The warm HDO/ H_2O ratio cannot be directly determined by comparing $X_{\text{in}}(\text{HDO})$ with the abundance of H_2^{18}O derived by

Persson et al. (2012), as the H_2 densities are estimated in different ways. It is, however, possible to estimate it using the HDO column density derived with our modeling in the warm inner regions of the envelope and the column density of water derived with interferometric observations of the para- H_2^{18}O $3_{1,3}-2_{2,0}$ transition at 203 GHz.

Including the 3σ uncertainties, we obtain a column density of HDO of about $(1.4-3.5) \times 10^{16} \text{ cm}^{-2}$ in the warm inner envelope ($T \geq 100 \text{ K}$) of IRAS 4A. The column density of p- H_2^{18}O is estimated by Taquet et al. (2013a) to be between 5.5×10^{15} and $1.5 \times 10^{16} \text{ cm}^{-2}$ for a hot corino size comparable to ours ($\sim 0.73''$, $\sim 85 \text{ AU}$). It is also consistent with the estimate of $7.9 \times 10^{15} \text{ cm}^{-2}$ by Persson et al. (2012) for the same object. Assuming an ortho-to-para ratio of water equal to 3 and an isotopic $\text{H}_2^{16}\text{O}/\text{H}_2^{18}\text{O}$ ratio of 500, we can consequently estimate the inner HDO/ H_2O ratio to be about $4 \times 10^{-4}-3.0 \times 10^{-3}$ in the warm envelope of IRAS 4A. This result is, however, lower than the estimate by Taquet et al. (2013a) of $5 \times 10^{-3}-3 \times 10^{-2}$. In IRAS 4B, we find a column density of deuterated water between 1.0×10^{15} and $3.0 \times 10^{16} \text{ cm}^{-2}$. Using the para- H_2^{18}O column density estimated by Jørgensen & van Dishoeck (2010b) at $4 \times 10^{15} \text{ cm}^{-2}$, the HDO/ H_2O ratio is then about $1 \times 10^{-4}-3.7 \times 10^{-3}$. A part of this range is consequently in agreement with the upper limit previously determined by Jørgensen & van Dishoeck (2010a, $\leq 6 \times 10^{-4}$). The range in HDO/ H_2O determined for IRAS 4B appears larger than for IRAS 4A because of the larger uncertainties obtained with the HDO inner abundances.

Table 4 summarizes the HDO/ H_2O ratios derived in Class 0 sources in this paper and in previous studies. The results found here seem to favor low values around 10^{-3} for the warm HDO/ H_2O ratios. We have to keep in mind that in our modeling, the HDO inner abundance is constrained thanks to

Table 4. Summary of the HDO/H₂O ratios determined in Class 0 protostars.

Source	Study ⁽¹⁾	Inner HDO/H ₂ O ratio	Outer HDO/H ₂ O ratio	Observations ⁽²⁾	Modeling ⁽³⁾
IRAS 16293-2422	a	3×10^{-2}	$\leq 2 \times 10^{-3}$	HDO: IRAM (4), JCMT (1) H ₂ ¹⁶ O: ISO (11)	1D, non-LTE
	b	4×10^{-3} – 5.1×10^{-2}	3×10^{-3} – 1.5×10^{-2}	HDO: HIFI (9), IRAM (3), JCMT (1) H ₂ ¹⁸ O: HIFI (5)	1D, non-LTE
	c	$(9.2 \pm 2.6) \times 10^{-4}$	–	HDO: SMA (1) H ₂ ¹⁸ O: ALMA (1), SMA (1)	0D, LTE
NGC 1333 IRAS2A	d	$\geq 1 \times 10^{-2}$	9×10^{-3} – 1.8×10^{-1}	HDO: IRAM (3), JCMT (1), APEX (1) H ₂ ¹⁸ O: HIFI* (non-detection) H ₂ ¹⁶ O: HIFI*	1D, non-LTE
	e	$\sim 1 \times 10^{-3}$	–	HDO: IRAM (1), H ₂ ¹⁸ O: PdBi (1), HIFI (1)	0D, LTE
	f	3×10^{-3} – 8×10^{-2}	–	HDO: PdBi (1), IRAM (3) H ₂ ¹⁸ O: PdBi (1)	0D, non-LTE
NGC 1333 IRAS4A	f	5×10^{-3} – 3×10^{-2}	–	HDO: PdBi (1) H ₂ ¹⁸ O: PdBi (1)	0D, non-LTE
	This paper	4×10^{-4} – 3.0×10^{-3}	about 10^{-2} ⁽⁴⁾	HDO: HIFI (1), IRAM (3), JCMT (1) H ₂ ¹⁸ O: PdBi* (1) H ₂ ¹⁶ O: HIFI* (4)	1D, non-LTE
NGC 1333 IRAS4B	g	$\leq 6 \times 10^{-4}$	–	HDO: SMA (non-detection) H ₂ ¹⁸ O: PdBi (1)	0D, non-LTE
	This paper	1×10^{-4} – 3.7×10^{-3}	–	HDO: HIFI (2), IRAM (2), APEX (1) H ₂ ¹⁸ O: PdBi* (1)	1D, non-LTE

Notes. ⁽¹⁾ References classified by order of publication for each source: a) Parise et al. (2005); Ceccarelli et al. (2000); b) Coutens et al. (2012, 2013); c) Persson et al. (2013); d) Liu et al. (2011); e) Visser et al. (2013); f) Taquet et al. (2013a); g) Jørgensen & van Dishoeck (2010a). ⁽²⁾ This column shows which tracers are used to determine the HDO/H₂O ratios, which telescopes the analysis is based on, and how many detected lines (number into brackets) of each tracer are used. The notation IRAM refers to the single-dish 30 m-telescope. The star (*) shows that the modeling of the water lines was not carried out in the study quoted in Col. 2, but come, as explained in the text, from the following papers: Jørgensen & van Dishoeck (2010a); Persson et al. (2012); Taquet et al. (2013a); Mottram et al. (2013). ⁽³⁾ This column describes the type of modeling used to determine the HDO/H₂O ratio: 0D or 1D structure and LTE or non-LTE analysis. ⁽⁴⁾ This value has to be confirmed using a HDO abundance profile similar to the H₂O profile in Mottram et al. (2013).

the HDO excited lines at 226 and 242 GHz. In Jørgensen & van Dishoeck (2010a), the non-detection of the line at 226 GHz with the SMA was used to determine an upper limit on the water D/H ratio. The use of the same lines explains easily why our results are in agreement with Jørgensen & van Dishoeck (2010a). Taquet et al. (2013a) used interferometric observations of the more excited HDO 4_{2,2}–4_{2,3} line at 144 GHz ($E_{\text{up}} = 319$ K) to derive the HDO/H₂O ratio using a non-LTE approach. These different results suggest that, depending on their excitation, the HDO lines could be emitted in different regions inside the hot corino where disks could be present. Observations at very high spatial resolution, such as with the Atacama Large Millimeter/Submillimeter Array (ALMA), as well as more complex modeling would then be required to answer this question. Another simpler explanation could arise from the H₂ density assumed in the hot corino. If the density used by Taquet et al. (2013a) were slightly higher, it could lead to a lower HDO/H₂O ratio, reconciling the results.

Assuming that the presence of HDO and H₂O in the warm inner envelope is only due to the desorption from the grains, grain-surface chemical models (Cazaux et al. 2011; Taquet et al. 2013b) can be used to determine the initial conditions (temperature and H₂ density) of the parent cloud leading to the HDO/H₂O ratios obtained here. The model by Cazaux et al. (2011), which studies the formation of deuterated ices by accreting species from the gas phase during a free-fall collapse, shows that low

temperatures (~ 12 K) are required to obtain HDO/H₂O ratios between 10^{-4} and a few 10^{-3} (see Fig. 4 in Coutens et al. 2013). The density is, however, not constrained. Additional information such as D₂O/H₂O ratios would be necessary to estimate it. The model by Taquet et al. (2013b), which follows the multilayer formation of deuterated ices with a pseudo time-dependent approach, confirms that the temperature should be low (~ 10 K) to obtain HDO/H₂O ratios close to 10^{-3} . Low densities ($\sim 10^3$ cm⁻³) would also be needed (see Fig. 2 in Taquet et al. 2013a).

4.2.2. Cold outer HDO/H₂O ratios

Mottram et al. (2013) studied several *Herschel*/HIFI water lines for deriving the H₂O abundance profile along the envelope of several low-mass protostars and in particular IRAS 4A. They showed that, in the colder envelope, an H₂O abundance profile with a gradual increase of the abundance with the radius is more consistent with the observations than a drop abundance profile as used here (see Fig. 14 in Mottram et al. 2013). Their best-fit obtained with the drop profile ($X_{\text{out}} = 3 \times 10^{-10}$ in the outer envelope and $X_{\text{abs}} = 3 \times 10^{-7}$, $N_{\text{abs}} = 1 \times 10^{15}$ cm⁻² in the absorbing layer) can, however, give some ideas on the order of magnitude of cold HDO/H₂O ratios. In IRAS 4A, the HDO/H₂O ratio is then estimated at about 4% in the outer envelope and

about 9×10^{-3} in the absorbing layer. The cold HDO/H₂O ratios therefore seem to be about a few percent and higher than the warm HDO/H₂O ratios. These results obviously have to be considered carefully, as it is shown that the H₂O lines are better fitted with a sloping abundance profile. A proper estimate of the HDO/H₂O ratio with similar abundance profiles for HDO and H₂O is therefore required to confirm the relatively high values of the cold HDO/H₂O ratios. These high estimates of the cold HDO/H₂O ratios are also in agreement with the cold ratios found in IRAS 16293-2422 by Coutens et al. (2012, $0.3\text{--}1.5 \times 10^{-2}$) and in NGC 1333 IRAS 2A by Liu et al. (2011, $0.9\text{--}18 \times 10^{-2}$). No analysis of the H₂O lines observed towards IRAS 4B was carried out; consequently, the cold HDO/H₂O ratio cannot be determined in this source at the moment.

In IRAS 4A, the cold HDO/H₂O ratio seems to be higher than the warm HDO/H₂O ratio. Similar conclusions were obtained by Coutens et al. (2013) with the study of the D₂O/H₂O ratio in IRAS 16293-2422. Different mechanisms were proposed to explain this difference. The first is that water could be formed differently in the warm and cold regions. We can imagine, for example, that, in addition to the desorption of the water molecules trapped in the icy grain mantles (thermal desorption in the hot corino and photodesorption in the outer envelope), water could also be formed in the gas phase through ion-molecule reactions in the cold outer envelope, giving a HDO/H₂O abundance ratio up to 1 (Roberts et al. 2004), and through neutral-neutral endothermic reactions in the warm regions, giving a HDO/H₂O abundance ratio of $10^{-3}\text{--}10^{-2}$ (Thi et al. 2010). As the D/H ratio would lead to a higher deuterium fractionation for cold environments, it could explain why the HDO/H₂O ratio is higher in the cold outer envelope. Self-shielding in the hot corino was also suggested in Coutens et al. (2013). Since H₂O is more abundant than its deuterated forms, it should self-shield first, reducing its photodissociation comparatively to HDO and D₂O. Another hypothesis is provided by chemical models including a multi-layer approach. Interstellar ices display a gradient of their deuterium fractionation, the D/H ratio increasing towards the surface of the ices. External ice layers are enriched in deuterium because they have been formed in prestellar cores where the gaseous D/H ratio is high, while the internal part of the ices have been formed in molecular cloud conditions with limited deuterium fractionation. The first outer layers, which are highly deuterated, are then evaporated in the outer envelope through non-thermal processes (photo-evaporation or reactive evaporation), whereas the less deuterated inner layers are only released in the gas phase in the warm envelope when the temperature reaches ~ 100 K (Taquet et al., in prep.). The difference in the HDO/H₂O ratio could then originate from the grain layer-structure.

5. Conclusions

Deuterated water was detected in the low-mass protostars NGC 1333 IRAS 4A and IRAS 4B with the *Herschel*/HIFI instrument, as well as with ground-based telescopes (IRAM, JCMT, and APEX). The HDO fundamental $1_{1,1}\text{--}0_{0,0}$ and $1_{0,1}\text{--}0_{0,0}$ transitions observed at 894 and 465 GHz, respectively, show a broad component tracing the outflows in addition to an inverse P-Cygni profile indicating infall motions in the protostellar envelope.

A RATRAN non-LTE model was then carried out to determine the HDO abundances in the protostellar envelope, after subtraction of the broad component observed on the line profiles. In IRAS 4A, the derived HDO abundances are about 7.5×10^{-9} in the warm inner regions of the envelope ($T > 100$ K) where

water molecules thermally desorb from the grain mantles, and about 1.2×10^{-11} in the outer envelope. In IRAS 4B, the inner abundance is about 1.0×10^{-8} , whereas the outer abundance is about 1.2×10^{-10} . Using the H₂¹⁸O column density determined thanks to the interferometric observations of the $3_{1,3}\text{--}2_{2,0}$ transition, we obtain in the warm inner regions HDO/H₂O ratios of about $4 \times 10^{-4}\text{--}3.0 \times 10^{-3}$ for IRAS 4A and $1 \times 10^{-4}\text{--}3.7 \times 10^{-3}$ for IRAS 4B. Comparing the HDO outer abundance with the H₂O abundance estimated by Mottram et al. (2013) in IRAS 4A, the outer HDO/H₂O ratio seems to be much higher (about a few percent) than in the hot corino. Several mechanisms were suggested in Sect. 4.2.2 to explain this variation.

The presence of an extended absorbing layer with a HDO column density of $\sim 1.4 \times 10^{13}$ cm⁻² is required to reproduce the deep absorbing components seen in the fundamental lines of both sources. Such a layer was already discovered around the low-mass protostar IRAS 16293-2422 (Coutens et al. 2012). This layer could then be ubiquitous in the surroundings of low-mass protostars. A narrow SiO emission line detected in the IRAS4 complex by Lefloch et al. (1998) appears at the same velocity as the HDO absorbing components and shows a similar linewidth, which could suggest a common origin of these two species (see Appendix B). Photodesorption mechanisms or sputtering due to decelerated shocks could release into the gas phase molecules of water and SiO contained in the grain mantles.

In the outflows, the HDO column density is estimated, using the RADEX non-LTE code, at $\sim (2\text{--}4) \times 10^{13}$ cm⁻², which leads to an abundance of about $(0.7\text{--}1.9) \times 10^{-9}$. The HDO/H₂O ratio is estimated at $\sim 1 \times 10^{-3}\text{--}9 \times 10^{-2}$ in the red part of the outflow and $7 \times 10^{-4}\text{--}6 \times 10^{-2}$ in the blue part. These results are consistent with the water deuterium fractionation in the warm inner regions of IRAS 4A derived here, and with the results of Taquet et al. (2013a). This could mean that water is released from the grain mantles by sputtering mechanisms in the outflows and by thermal desorption in the hot corino, supporting an early formation of H₂O and HDO during the star formation. However, the wide range of values determined in the outflows does not allow us to clearly assert it.

Finally, we also compared the HDO abundances derived in low-mass protostars. The outer abundances are particularly well constrained by the HDO $1_{1,1}\text{--}0_{0,0}$ line observed at 894 GHz with *Herschel*/HIFI. The source NGC 1333 IRAS 4A shows the lowest HDO abundances among the low-mass protostars. But the range of HDO outer abundances is relatively narrow, between 10^{-11} and a few 10^{-10} . A correlation is observed between the ratio of the inner and outer abundances and the submillimeter luminosity, but more observations on a larger sample are required to confirm this correlation. For the same region, the HDO outer abundances also seem to vary with the submillimeter luminosity, which could reflect a more efficient non-thermal desorption in less dense envelopes.

Acknowledgements. The authors thank D. C. Lis for his comments on the manuscript. HIFI has been designed and built by a consortium of institutes and university departments from across Europe, Canada, and the United States under the leadership of SRON Netherlands Institute for Space Research, Groningen, The Netherlands, and with major contributions from Germany, France, and the US. Consortium members are: Canada: CSA, U. Waterloo; France: IRAP (formerly CESR), LAB, LERMA, IRAM; Germany: KOSMA, MPIfR, MPS; Ireland, NUI Maynooth; Italy: ASI, IFSI-INAF, Osservatorio Astrofisico di Arcetri-INAF; Netherlands: SRON, TUD; Poland: CAMK, CBK; Spain: Observatorio Astronómico Nacional (IGN), Centro de Astrobiología (CSIC-INTA). Sweden: Chalmers University of Technology – MC2, RSS & GARD; Onsala Space Observatory; Swedish National Space Board, Stockholm University – Stockholm Observatory; Switzerland: ETH Zurich, FHNW; USA: Caltech, JPL, NHSC.

References

- André, P., Ward-Thompson, D., & Barsony, M. 1993, *ApJ*, 406, 122
- Belloche, A., Hennebelle, P., & André, P. 2006, *A&A*, 453, 145
- Bergin, E. A., Phillips, T. G., Comito, C., et al. 2010, *A&A*, 521, L20
- Blake, G. A., Sandell, G., van Dishoeck, E. F., et al. 1995, *ApJ*, 441, 689
- Bockelée-Morvan, D., Gautier, D., Lis, D. C., et al. 1998, *Icarus*, 133, 147
- Bontemps, S., André, P., Terebey, S., & Cabrit, S. 1996, *A&A*, 311, 858
- Bottinelli, S., Ceccarelli, C., Lefloch, B., et al. 2004, *ApJ*, 615, 354
- Bottinelli, S., Ceccarelli, C., Williams, J. P., & Lefloch, B. 2007, *A&A*, 463, 601
- Campins, H., & Lauretta, D. S. 2004, in *AAS/Division for Planetary Sciences Meeting Abstracts #36*, BAAS, 36, 1118
- Caselli, P., Hartquist, T. W., & Havnes, O. 1997, *A&A*, 322, 296
- Caselli, P., Keto, E., Bergin, E. A., et al. 2012, *ApJ*, 759, L37
- Cazaux, S., Cobut, V., Marseille, M., Spaans, M., & Caselli, P. 2010, *A&A*, 522, A74
- Cazaux, S., Caselli, P., & Spaans, M. 2011, *ApJ*, 741, L34
- Ceccarelli, C., Hollenbach, D. J., & Tielens, A. G. G. M. 1996, *ApJ*, 471, 400
- Ceccarelli, C., Castets, A., Caux, E., et al. 2000, *A&A*, 355, 1129
- Ceccarelli, C., Bacmann, A., Boogert, A., et al. 2010, *A&A*, 521, L22
- Choi, M. 2001, *ApJ*, 553, 219
- Choi, M. 2005, *ApJ*, 630, 976
- Choi, M., Kamazaki, T., Tatematsu, K., & Panis, J.-F. 2004, *ApJ*, 617, 1157
- Codella, C., Bachiller, R., & Reipurth, B. 1999, *A&A*, 343, 585
- Codella, C., Ceccarelli, C., Nisini, B., et al. 2010, *A&A*, 522, L1
- Coutens, A., Vastel, C., Caux, E., et al. 2012, *A&A*, 539, A132
- Coutens, A., Vastel, C., Cazaux, S., et al. 2013, *A&A*, 553, A75
- Crimier, N., Ceccarelli, C., Maret, S., et al. 2010, *A&A*, 519, A65
- Curtis, E. I., Richer, J. S., & Buckle, J. V. 2010, *MNRAS*, 401, 455
- Dalgarno, A. 1980, in *Interstellar Molecules*, ed. B. H. Andrew, *IAU Symp.*, 87, 273
- Dartois, E., Thi, W.-F., Geballe, T. R., et al. 2003, *A&A*, 399, 1009
- de Graauw, T., Helmich, F. P., Phillips, T. G., et al. 2010, *A&A*, 518, L6
- Di Francesco, J., Myers, P. C., Wilner, D. J., Ohashi, N., & Mardones, D. 2001, *ApJ*, 562, 770
- Drake, M. J., & Campins, H. 2006, in *Asteroids, Comets, Meteors*, eds. L. Daniela, M. Sylvio Ferraz, & F. J. Angel, *IAU Symp.*, 229, 381
- Dulieu, F., Amiaud, L., Congiu, E., et al. 2010, *A&A*, 512, A30
- Evans, II, N. J., Dunham, M. M., Jørgensen, J. K., et al. 2009, *ApJS*, 181, 321
- Faure, A., Wiesenfeld, L., Scribano, Y., & Ceccarelli, C. 2011, *MNRAS*, 2015
- Flower, D. R., & Pineau des Forêts, G. 1994, *MNRAS*, 268, 724
- Fraser, H. J., Collings, M. P., McCoustra, M. R. S., & Williams, D. A. 2001, *MNRAS*, 327, 1165
- Froebrich, D. 2005, *ApJS*, 156, 169
- Geiss, J., & Gloeckler, G. 1998, *Space Sci. Rev.*, 84, 239
- Genda, H., & Ikoma, M. 2008, *Icarus*, 194, 42
- Gibb, A. G., Richer, J. S., Chandler, C. J., & Davis, C. J. 2004, *ApJ*, 603, 198
- Guillet, V., Jones, A. P., & Pineau Des Forêts, G. 2009, *A&A*, 497, 145
- Gusdorf, A., Cabrit, S., Flower, D. R., & Pineau Des Forêts, G. 2008a, *A&A*, 482, 809
- Gusdorf, A., Pineau Des Forêts, G., Cabrit, S., & Flower, D. R. 2008b, *A&A*, 490, 695
- Haas, M. R., Hollenbach, D. J., & Erickson, E. F. 1986, *ApJ*, 301, L57
- Hartogh, P., Lis, D. C., Bockelée-Morvan, D., et al. 2011, *Nature*, 478, 218
- Hirota, T., Bushimata, T., Choi, Y. K., et al. 2008, *PASJ*, 60, 37
- Hogerheijde, M. R., & van der Tak, F. F. S. 2000, *A&A*, 362, 697
- Hollenbach, D., & McKee, C. F. 1979, *ApJS*, 41, 555
- Hollenbach, D., Kaufman, M. J., Bergin, E. A., & Melnick, G. J. 2009, *ApJ*, 690, 1497
- Ikoma, M., & Genda, H. 2006, *LPI Contributions*, 1335, 50
- Ioppolo, S., Cuppen, H. M., Romanzin, C., van Dishoeck, E. F., & Linnartz, H. 2008, *ApJ*, 686, 1474
- Jensen, M. J., Bilodeau, R. C., Safvan, C. P., et al. 2000, *ApJ*, 543, 764
- Jiménez-Serra, I., Martín-Pintado, J., Rodríguez-Franco, A., & Marcelino, N. 2004, *ApJ*, 603, L49
- Jiménez-Serra, I., Caselli, P., Tan, J. C., et al. 2010, *MNRAS*, 406, 187
- Jiménez-Serra, I., Martín-Pintado, J., Winters, J.-M., Rodríguez-Franco, A., & Caselli, P. 2011, *ApJ*, 739, 80
- Jørgensen, J. K., & van Dishoeck, E. F. 2010a, *ApJ*, 725, L172
- Jørgensen, J. K., & van Dishoeck, E. F. 2010b, *ApJ*, 710, L72
- Jørgensen, J. K., Schöier, F. L., & van Dishoeck, E. F. 2002, *A&A*, 389, 908
- Jørgensen, J. K., Hogerheijde, M. R., van Dishoeck, E. F., Blake, G. A., & Schöier, F. L. 2004, *A&A*, 413, 993
- Jørgensen, J. K., Bourke, T. L., Myers, P. C., et al. 2007, *ApJ*, 659, 479
- Jørgensen, J. K., van Dishoeck, E. F., Visser, R., et al. 2009, *A&A*, 507, 861
- Karska, A., Herczeg, G. J., van Dishoeck, E. F., et al. 2013, *A&A*, 552, A141
- Kristensen, L. E., Visser, R., van Dishoeck, E. F., et al. 2010, *A&A*, 521, L30
- Kristensen, L. E., van Dishoeck, E. F., Bergin, E. A., et al. 2012, *A&A*, 542, A8
- Langer, W. D., Castets, A., & Lefloch, B. 1996, *ApJ*, 471, L111
- Lay, O. P., Carlstrom, J. E., & Hills, R. E. 1995, *ApJ*, 452, L73
- Lecuyer, C., Gillet, P., & Robert, F. 1998, *Chem. Geol.*, 145, 249
- Lefloch, B., Castets, A., Cernicharo, J., & Loinard, L. 1998, *ApJ*, 504, L109
- Lefloch, B., Cabrit, S., Codella, C., et al. 2010, *A&A*, 518, L113
- Levenberg, K. 1944, *Quart. Appl. Math.*, 2, 164
- Liu, F., Parise, B., Kristensen, L., et al. 2011, *A&A*, 527, A19
- Lunine, J. I., Chambers, J., Morbidelli, A., & Leshin, L. A. 2003, *Icarus*, 165, 1
- Maret, S., Ceccarelli, C., Caux, E., Tielens, A. G. G. M., & Castets, A. 2002, *A&A*, 395, 573
- Marquardt, D. 1963, *SIAM J. Appl. Math.*, 11, 431
- Meier, R., Owen, T. C., Matthews, H. E., et al. 1998, *Science*, 279, 842
- Miller, A., Lauroesch, J. T., Sofia, U. J., Cartledge, S. I. B., & Meyer, D. M. 2007, *ApJ*, 659, 441
- Miyauchi, N., Hidaka, H., Chigai, T., et al. 2008, *Chem. Phys. Lett.*, 456, 27
- Morbidelli, A., Chambers, J., Lunine, J. I., et al. 2000, *Meteoritics and Planetary Science*, 35, 1309
- Morton, D. C. 1975, *ApJ*, 197, 85
- Mottram, J. C., van Dishoeck, E. F., Schmalzl, M., et al. 2013, *A&A*, 558, A126
- Myers, P. C., & Ladd, E. F. 1993, *ApJ*, 413, L47
- Niemann, H. B., Atreya, S. K., Carignan, G. R., et al. 1996, *Science*, 272, 846
- Öberg, K. I., Linnartz, H., Visser, R., & van Dishoeck, E. F. 2009, *ApJ*, 693, 1209
- O'Brien, D. P., Morbidelli, A., & Levison, H. F. 2006, in *37th Annual Lunar and Planetary Science Conference*, eds. S. Mackwell, & E. Stansbery, *Lunar and Planetary Inst. Technical Report*, 37, 2347
- Ossenkopf, V., & Henning, T. 1994, *A&A*, 291, 943
- Ott, S. 2010, in *Astronomical Data Analysis Software and Systems XIX*, *ASP Conf. Ser.*, 434, 139
- Parise, B., Simon, T., Caux, E., et al. 2003, *A&A*, 410, 897
- Parise, B., Caux, E., Castets, A., et al. 2005, *A&A*, 431, 547
- Persson, M. V., Jørgensen, J. K., & van Dishoeck, E. F. 2012, *A&A*, 541, A39
- Persson, M. V., Jørgensen, J. K., & van Dishoeck, E. F. 2013, *A&A*, 549, L3
- Phillips, T. G., & Vastel, C. 2003, in *SFChem 2002: Chemistry as a Diagnostic of Star Formation*, eds. C. L. Curry, & M. Fich, 3
- Pickett, H. M., Poynter, R. L., Cohen, E. A., et al. 1998, *J. Quant. Spectr. Rad. Transf.*, 60, 883
- Pilbratt, G. L., Riedinger, J. R., Passvogel, T., et al. 2010, *A&A*, 518, L1
- Pineda, J. E., Maury, A. J., Fuller, G. A., et al. 2012, *A&A*, 544, L7
- Raymond, S. N., Quinn, T., & Lunine, J. I. 2004, *Icarus*, 168, 1
- Raymond, S. N., Quinn, T., & Lunine, J. I. 2006, *Icarus*, 183, 265
- Raymond, S. N., O'Brien, D. P., Morbidelli, A., & Kaib, N. A. 2009, *Icarus*, 203, 644
- Roberts, H., Herbst, E., & Millar, T. J. 2004, *A&A*, 424, 905
- Roberts, J. F., Jiménez-Serra, I., Gusdorf, A., & Martín-Pintado, J. 2012, *A&A*, 544, A150
- Roelfsema, P. R., Helmich, F. P., Teyssier, D., et al. 2012, *A&A*, 537, A17
- Sakai, N., Sakai, T., & Yamamoto, S. 2006, *PASJ*, 58, L15
- Schilke, P., Walmsley, C. M., Pineau des Forêts, G., & Flower, D. R. 1997, *A&A*, 321, 293
- Schilke, P., Pineau des Forêts, G., Walmsley, C. M., & Martín-Pintado, J. 2001, *A&A*, 372, 291
- Sofia, U. J., Cardelli, J. A., & Savage, B. D. 1994, *ApJ*, 430, 650
- Stimpfl, M., Lauretta, D. S., & Drake, M. J. 2004, *Meteoritics and Planetary Science Supplement*, 39, 5218
- Tafalla, M., Santiago-García, J., Hacar, A., & Bachiller, R. 2010, *A&A*, 522, A91
- Taquet, V., López-Sepulcre, A., Ceccarelli, C., et al. 2013a, *ApJ*, 768, L29
- Taquet, V., Peters, P. S., Kahane, C., et al. 2013b, *A&A*, 550, A127
- Thi, W.-F., Woitke, P., & Kamp, I. 2010, *MNRAS*, 407, 232
- Tielens, A. G. G. M., & Hagen, W. 1982, *A&A*, 114, 245
- van der Tak, F. F. S., Black, J. H., Schöier, F. L., Jansen, D. J., & van Dishoeck, E. F. 2007, *A&A*, 468, 627
- van Dishoeck, E. F., Kristensen, L. E., Benz, A. O., et al. 2011, *PASP*, 123, 138
- Vastel, C., Ceccarelli, C., Caux, E., et al. 2010, *A&A*, 521, L31
- Villanueva, G. L., Mumma, M. J., Bonev, B. P., et al. 2009, *ApJ*, 690, L5
- Visser, R., Jørgensen, J. K., Kristensen, L. E., van Dishoeck, E. F., & Bergin, E. A. 2013, *ApJ*, 769, 19
- Vuong, M. H., Montmerle, T., Grosso, N., et al. 2003, *A&A*, 408, 581
- Wagner, A. F., & Graff, M. M. 1987, *ApJ*, 317, 423
- Walmsley, C. M., Pineau des Forêts, G., & Flower, D. R. 1999, *A&A*, 342, 542
- Walsh, A. J., Bourke, T. L., & Myers, P. C. 2006, *ApJ*, 637, 860
- Wiesenfeld, L., Scribano, Y., & Faure, A. 2011, *Physical Chemistry Chemical Physics (Incorporating Faraday Transactions)*, 13, 8230
- Yildiz, U. A., Kristensen, L. E., van Dishoeck, E. F., et al. 2012, *A&A*, 542, A86
- Yildiz, U. A., Acharyya, K., Goldsmith, P. F., et al. 2013, *A&A*, 558, A58

-
- ¹ Université de Toulouse, UPS-OMP, IRAP, Toulouse, France
e-mail: acoutens@nbi.dk
- ² CNRS, IRAP, 9 Av. Colonel Roche, BP 44346, 31028 Toulouse Cedex 4, France
- ³ Niels Bohr Institute, University of Copenhagen, Juliane Maries Vej 30, 2100 Copenhagen Ø., Denmark
- ⁴ Centre for Star and Planet Formation, Natural History Museum of Denmark, University of Copenhagen, Øster Voldgade 57, 1350 Copenhagen K., Denmark
- ⁵ LERMA, Observatoire de Paris, UMR 8112 CNRS/INSU, 61 Av. de l'Observatoire, 75014 Paris, France
- ⁶ INAF – Osservatorio Astrofisico di Arcetri, Largo E. Fermi 5, 50125 Firenze, Italy
- ⁷ Harvard-Smithsonian Center for Astrophysics, 60 Garden Street, Cambridge, MA 02138, USA
- ⁸ Institut de Planétologie et d'Astrophysique de Grenoble (IPAG), UMR 5274, UJF-Grenoble 1/CNRS, 38041 Grenoble, France
- ⁹ Leiden Observatory, Leiden University, PO Box 9513, 2300 RA Leiden, The Netherlands
- ¹⁰ Max-Planck-Institut für Extraterrestrische Physik, Giessenbachstrasse 1, 85748 Garching, Germany
- ¹¹ California Institute of Technology, Infrared Processing and Analysis Center, Mail Code 100-22, Pasadena, CA 91125, USA
- ¹² Université de Bordeaux, Laboratoire d'Astrophysique de Bordeaux, 33000 Bordeaux, France
- ¹³ CNRS/INSU, UMR 5804, BP 89, 33271 Floirac Cedex, France
- ¹⁴ Physikalisches Institut, Universität zu Köln, Zùlpicher Str. 77, 50937 Köln, Germany
- ¹⁵ Max-Planck-Institut für Radioastronomie, Auf dem Hügel 69, 53121 Bonn, Germany
- ¹⁶ University of Waterloo, Department of Physics and Astronomy, Waterloo, Ontario, Canada
- ¹⁷ NASA Postdoctoral Program Fellow, NASA Goddard Space Flight Center, 8800 Greenbelt Road, Greenbelt, MD 20770, USA
- ¹⁸ SRON Netherlands Institute for Space Research, Landleven 12, 9747 AD Groningen, The Netherlands
- ¹⁹ Kapteyn Astronomical Institute, University of Groningen, 9700 AV Groningen, The Netherlands
- ²⁰ Department of Astronomy, University of Michigan, 500 Church Street, Ann Arbor, MI 48109-1042, USA

Appendix A: *Herschel*/HIFI observations

Table A.1. List of the *Herschel*/HIFI obsIDs.

Source	HDO $1_{1,1}-0_{0,0}$	HDO $2_{1,1}-2_{0,2}$
NGC 1333 IRAS 4A	1342225938	1342225931
NGC 1333 IRAS 4B	1342225940	1342225933
Red outflow IRAS 4A	1342225939	1342225932

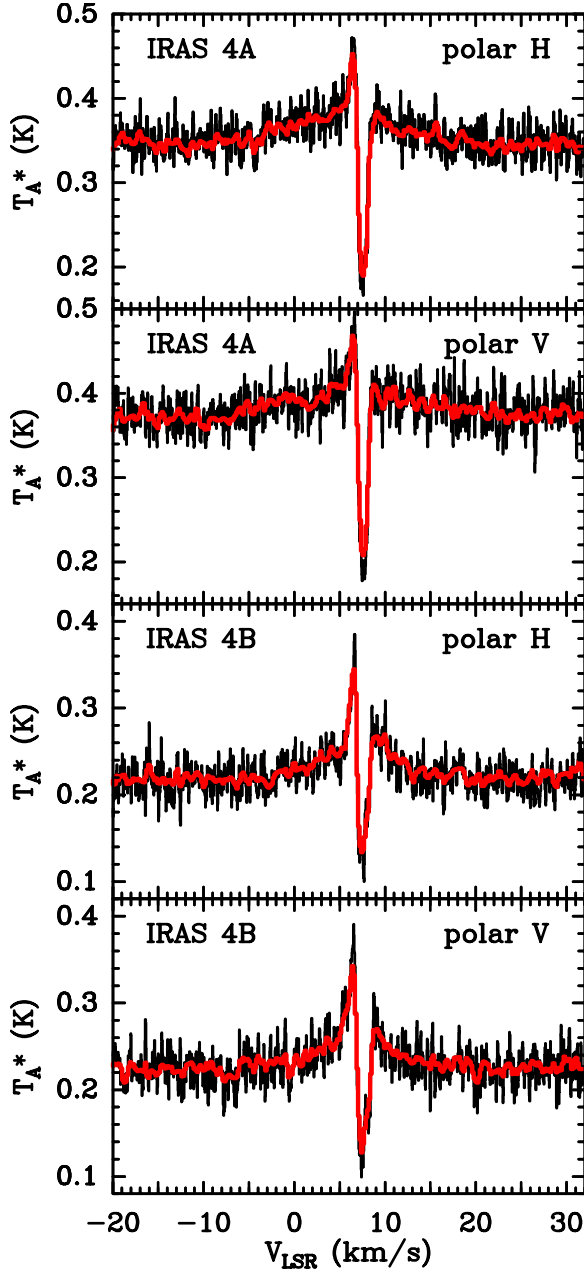


Fig. A.1. Comparison of the WBS (red) and HRS (black) spectra obtained at 894 GHz with *Herschel*/HIFI towards IRAS 4A and IRAS 4B for the H and V polarizations.

Appendix B: SiO and HDO: The same origin?

The present observations towards the IRAS 4 region reveal an interesting similarity between the deep absorbing components of HDO and the narrow SiO emission line detected by Lefloch et al. (1998). The latter shows a velocity and a linewidth consistent with the HDO absorbing component (see Fig. B.1), which could

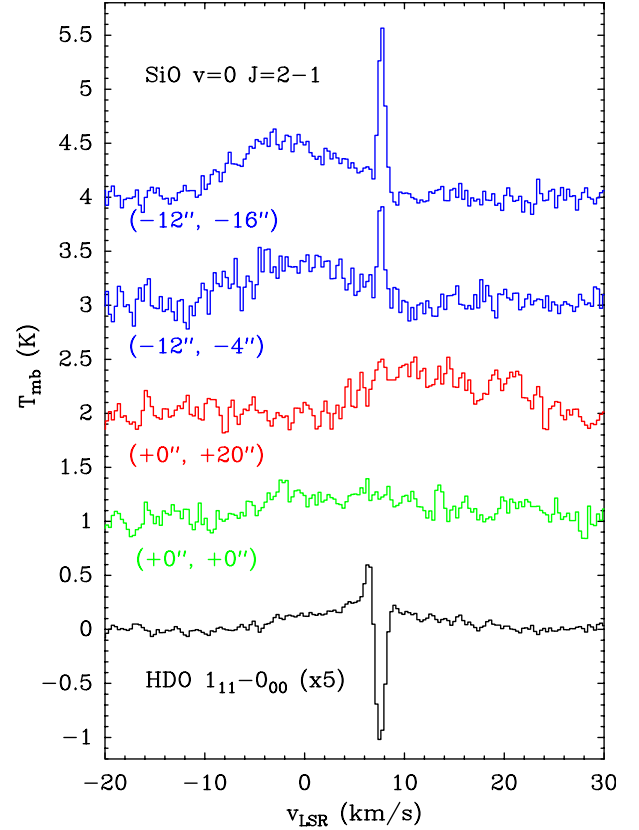


Fig. B.1. Comparison of the HDO $1_{1,1}-0_{0,0}$ transition (black) observed towards IRAS 4A and the SiO $v=0$ $J=2-1$ line observed towards IRAS 4A (green), a position in the red part of the outflow (red, position $(+0'', +20'')$ with respect to IRAS4A) and two positions in the blue part of the outflow (blue, upper spectra: position $(-12'', -16'')$, lower spectra: position $(-12'', -4'')$). The narrow emission line of SiO appears at the same velocity as the thin absorbing layer of HDO.

suggest a common origin. The narrow SiO emission is quite extended ($\sim 200''$, see Fig. 2 in Lefloch et al. 1998), as we have also inferred for the HDO absorbing layer (see Sect. 3.3). Variations of the narrow SiO line intensity are observed along the NGC 1333 complex, with particularly bright lines around the blue lobe and non-detections towards the source and the red lobe. From LVG (Large Velocity Gradient) modeling of the bright SiO narrow components in the blue lobe, Lefloch et al. (1998) estimated the SiO column density of $(1-5) \times 10^{12} \text{ cm}^{-2}$ and the H_2 density at about $(1-5) \times 10^5 \text{ cm}^{-3}$, assuming a gas temperature of 33 K equal to that of the dust. For the same SiO column density and a lower H_2 density ($\sim 10^4 \text{ cm}^{-3}$), the intensity of the SiO $v=0$ $J=2-1$ line is only 0.07 K, in agreement with the non-detection by Lefloch et al. of narrow SiO emission towards our HDO spectra positions ($\lesssim 0.27$ K for both the source position and the red lobe). To reproduce the HDO absorbing components with the RATRAN modeling, it is also necessary to restrain the H_2 density at a lower value ($< 10^5 \text{ cm}^{-3}$; see Sect. 3.3). A layer of constant column density but subject to density variations ($n(\text{H}_2) < 10^5 \text{ cm}^{-3}$ towards the sources and the red lobe and $n(\text{H}_2) \sim (1-5) \times 10^5 \text{ cm}^{-3}$ towards the blue lobe) could then explain both the deep HDO absorptions and the lack of detectable SiO narrow emission towards the sources and the red lobe as well as the bright SiO narrow emission towards the blue lobe. Alternatively, a layer of uniform low density $\sim 10^4 \text{ cm}^{-3}$, but with gas temperature locally increasing to $\sim 80-100$ K towards the blue lobe, would explain why SiO is only detected in this region. In these cases, the HDO absorptions should be shallower

towards the blue part of the outflow. Unfortunately, no HDO observation is available at this position to confirm it. Assuming that the HDO column density of the absorbing layer does not vary significantly between IRAS 4A and the blue outflow lobe, the SiO/HDO abundance ratio in this layer would be $\sim 0.07\text{--}0.35$. The beam sizes of the HDO $1_{1,1}\text{--}0_{0,0}$ line at 894 GHz and the SiO $v = 0, J = 2\text{--}1$ transition mapped by Lefloch et al. (1998) with the IRAM-30 m telescope are similar.

Another argument suggesting that the narrow HDO and SiO components may trace the same layer is that, in dense and dark clouds, both of these species are believed to be mostly trapped in dust grains and their associated icy mantles. Hence, the same mechanism could release SiO (or other Si components) at the same time as HDO and H₂O into the gas phase. We discuss below two mechanisms able to release these molecules into the gas phase: photodesorption and shocks. Another mechanism proposed by Yıldız et al. (2012) to explain detections of narrow ¹³CO emission lines within the outflow lobes of IRAS 4A is UV-heating by the central source. The narrow SiO emission in NGC 1333 has a more extended spatial distribution, which instead tends to peak outside of the outflow cavities (see Fig. 1 in Lefloch et al. 1998), which appears to rule out this interpretation here.

B.1. Photodesorption

It was suggested that narrow SiO emission at the systemic velocity could be produced by photodesorption mechanisms in photodissociation regions (PDR) such as the Orion bar (Walmsley et al. 1999; Schilke et al. 2001). Indeed, the strength of Si⁺ in irradiated regions suggests that up to $\sim 10\%$ of the elemental silicon is not locked in silicate grain cores, but in less refractory material that gets efficiently desorbed at low A_V (Haas et al. 1986). We note that a similar fraction of silicon ($\sim 5\%$) with respect to the cosmic abundance ($\sim 3 \times 10^{-5}$) is measured in the gas-phase of diffuse clouds (e.g., Morton 1975; Sofia et al. 1994; Miller et al. 2007). Gusdorf et al. (2008b) also estimated that, to account for the observed SiO line intensities in the blue lobe of L1157, about $\sim 10\%$ of the silicon assumed in the form of SiO has to be locked in the grain mantles.

Photodesorption could then release SiO in the gas phase simultaneously with water and HDO. Alternatively, the material could be trapped in grain mantles in the form of atomic Si; the Si would then be desorbed and react with O₂ or OH to form SiO according to the following reactions (Walmsley et al. 1999):



The balance between photodesorption and photodissociation predicts an SiO-enriched layer located at some depth behind the photodissociation front, which can easily explain the SiO column density observed towards the Orion Bar of a few 10^{12} cm^{-2} (Walmsley et al. 1999; Schilke et al. 2001). Although O₂ is actually less abundant than assumed in these early models, a tentative detection of O₂ was recently reported towards IRAS 4A at a velocity ($\sim 8.0 \text{ km s}^{-1}$) close to our HDO absorptions ($\sim 7.6 \text{ km s}^{-1}$), and suggested to be produced by photodesorption mechanisms (Yıldız et al. 2013). Photodissociation of H₂O would also produce ample OH to react with Si and form SiO by the second reaction above.

Photodesorption of grain mantles thus appears as a possible explanation for the narrow HDO and SiO components at the systemic velocity towards the IRAS 4A region. Photodissociation region models appropriate for the surface of

the NGC 1333 cloud, i.e., with lower UV radiation field ($\chi \sim 1$) than the Orion bar ($\chi \sim 10^4\text{--}10^5$), could verify if this mechanism also reproduces the observed SiO/HDO ratio.

B.2. Shocks

Shocks are another non-thermal mechanism able to remove both silicon and water from dust grains. Contrary to CO that traces all of the entrained material in molecular flows, broad SiO emission is mostly detected in the youngest outflows from Class 0 protostars (Gibb et al. 2004). This is not surprising, as SiO requires a higher density than CO for excitation and especially shocks fast enough ($\geq 10\text{--}25 \text{ km s}^{-1}$) to efficiently sputter SiO and Si from the mantles and grain cores in which they would otherwise remain locked (Schilke et al. 1997; Caselli et al. 1997; Gusdorf et al. 2008a,b; Guillet et al. 2009). Sputtering processes also efficiently release water ice from grain mantles, as illustrated, for example, by the similarity of the SiO and H₂O high-velocity wings in the L1157 outflow (Lefloch et al. 2010), and the broad wings in the HDO profile towards IRAS 4A (see Fig. B.1). The IRAS 4A outflow wings have a total SiO column density of a few 10^{13} cm^{-2} and an abundance relative to CO $\sim 3 \times 10^{-4}$ (Lefloch et al. 1998), typical of young outflows (Tafalla et al. 2010). The narrow SiO component towards IRAS 4A has a column density that is 10 times smaller than the column density in the broad SiO component, and an abundance relative to CO that is 100 times lower, when compared to the total C¹⁸O at systemic velocity (Lefloch et al. 1998). Hence, the presence of the narrow SiO and HDO components could be explained in this context if about 10% of the SiO (and HDO) released in outflow shocks suffered strong deceleration and chemical dilution (by a typical factor of 10–100) due to turbulent mixing with static ambient gas (Lefloch et al. 1998; Codella et al. 1999). The surface dilution induced by the mixing process would be compensated by the contribution of neighboring outflows, which cover a large fraction of the surface area in NGC 1333. The SiO/HDO ratio is estimated in the outflows at $0.25\text{--}1.5$ (using $N(\text{SiO}) = 1\text{--}3 \times 10^{13} \text{ cm}^{-2}$ from Lefloch et al. 1998 and $N(\text{HDO}) = 2\text{--}4 \times 10^{13} \text{ cm}^{-2}$ from Sect. 3.4). This could be consistent with that estimated for the narrow layer (0.07–0.35), raising the possibility that shocked gas could contribute to this extended SiO/HDO layer. The SiO and HDO molecules will then re-deplete onto grain mantles on timescales depending on the volume densities ($\sim 10^4$ years for densities about 10^5 cm^{-3} and $\sim 10^5$ years for densities about 10^4 cm^{-3}). Numerical simulations would be helpful to compare the predicted SiO/HDO ratio with the observations as well as to verify that sufficient deceleration can indeed be reached before SiO and HDO are readsorbed onto the grains to produce narrow SiO and HDO features close to systemic velocity.

Interactions of magnetic and/or radiative shock precursors with the ambient pre-shocked clumpy medium were also mentioned as a potential mechanism leading to the emission of narrow SiO lines (Jiménez-Serra et al. 2004, 2010, 2011). This interpretation was supported by the higher degree of excitation of the ion fluid compared to the neutral fluid towards the protostar L1448-mm. Roberts et al. (2012) showed, however, that the higher excitation of H¹³CO⁺ in the narrow component is not a conclusive indication of a precursor (it could simply be due to protostellar heating). This interpretation then relies entirely on the fact that the narrow SiO emission is compact and spatially confined to the regions around protostars. In the NGC 1333 complex, the narrow SiO component is spatially extended over the whole region (Lefloch et al. 1998). Therefore, the shock precursor interpretation would not hold here.